APPLICATION OF RUTHENIUM(II) POLY-BIS(TERPYRIDYL) MOLECULAR WIRES IN SOLID-STATE DYE-SENSITIZED SOLAR CELLS

A Thesis

Presented to

The Faculty of the Department of Chemistry and Biochemistry

California State University, Los Angeles

In Partial Fulfillment

of the Requirements for the Degree

Master of Arts Science

in

Chemistry

By

Jesus Corona

August 2025

The thesis of Jesus Corona is approved.

Dr. Yangyang Liu, Committee Chair

Dr. Dianlu Jiang

Dr. Matthias Selke

Dr. Chris Bachman

Dr. Krishna Foster, Department Chair

California State University, Los Angeles

June 2025

ABSTRACT

Application of Ruthenium(II) Poly-bis(terpyridyl) Molecular Wires in Solid-State Dye-Sensitized Solar Cells

By

Jesus Corona

Whether it's to mitigate the effects of climate change or decrease environmental pollution, energy production is on a trajectory away from conventional methods, such as the burning of fossil fuels and natural gases, towards more sustainable options. However, technologies capable of harnessing renewable resources are limited and presently insufficient at meeting current and exponentially increasing energy demands; thus, research focused on developing these technologies is crucial. Amongst these technologies, photovoltaics shows promise as potential alternatives as power conversion efficiencies (PCE) are consistently increasing and they utilize the most abundant renewable resource, the solar resource, to convert electromagnetic radiation into usable energy. Silicon based photovoltaics are currently the most prominent due to their relatively high PCEs. However, high purity requirements make fabrication economically and energetically expensive.

Although not as efficient, solid-state dye-sensitized solar cells (ssDSSCs) have demonstrated great potential as cheaper alternatives to conventional silicon photovoltaics. In this work, molecular wires comprised of ruthenium(II) (Ru^{II}) and 1,4-di([2,2':6',2''-terpyridin]-4'-yl) benzene (tpy-ph-tpy) are used sensitizers in ssDSSCs. Suitable HOMO and LUMO energy levels of $[Ru^{II}\text{-tpy-ph-tpy}]_n(2X)_n$ ($X = Cl^-$ or PF_6^-) were determined via UV-vis spectroscopy and cyclic voltammetry. By varying the ssDSSC fabrication

methods, efficiencies improved from 2.48×10^{-4}% to 1.62×10^{-2}%. Solar cell performance was characterized via open-circuit voltage decay (OCVD), electron lifetime (τ_n) and recombination order (β) measurements.

ACKNOWLEDGMENTS

This research would not be possible without the support and opportunities provided by several individuals. First and foremost, I would like to thank Dr. Liu for allowing me to begin my research journey as an undergraduate and for allowing me to continue as a graduate student under her guidance. I would also like to thank Dr. Jiang for his patience and availability – if not for him, my understanding of the project would be far more limited. I would like to thank Dr. Selke for the lessons I learned in his classes – the lessons he taught have provided me with a solid foundation to build upon. I would like to thank Dr. Bachman for agreeing to be a part of my thesis committee. I would also like to thank the members of the Liu lab for their friendship and support, especially my mentor, Akilah Miller, who guided me as I conducted research for the first time, and Tommy Taing. I would also like to acknowledge my friends and family for their continued support in all areas of life. Thank you for believing in me.

This research was funded by the NSF CREST program, the Center for Advancement toward Sustainable Urban Systems or CATSUS (HRD-2112554). I also acknowledge support from the U.S. Department of Energy (Award # DE-FE0032202).

TABLE OF CONTENTS

LIST OF TABLES

Table

LIST OF FIGURES

Figure

CHAPTER 1

INTRODUCTION

1.1 Solar Cells

Solar cells are photovoltaic (PV) devices that convert incident light into electric current through the photovoltaic effect; a phenomenon that was discovered in 1839 by French physicist Edmund Becquerel when he observed the generation of an electric current through the unsymmetric illumination of one of two similar electrodes, platinum, gold, brass, or silver-silver halide, submerged in dilute acid.[1] Proceeding work derived from this observation led research into semiconductor materials and eventually resulted in the first gold coated selenium solar cell by Charles E. Fritts in 1883.[2] The efficiency of selenium solar cells, as well as of other materials being investigated in the subsequent decades, remained stagnant at less than 1% until the development of crystalline silicon (c-Si) solar cells by Bell Laboratories in the 1940s.[3] Although early iterations of c-Si based solar cells also suffered from low efficiencies, control over the p-n junction propelled c-Si solar cell research in the following decades to achieve efficiencies of over 20%.

The success of c-Si solar cells spurred interest in the research of other novel materials for photovoltaic applications. Currently, solar cells can be grouped into five types of PV technologies: multijunction, single-junction gallium arsenide, c-Si, thin-film, and hybrid cells, as well as other emerging types of PVs (figure 1).[4] All of these solar cells utilize the photovoltaic effect; however, their working principles and efficiencies vary. The highest performing c-Si solar cells had an efficiency of 27.6% while the most efficient solar cell to date is a III-V multijunction solar cell equipped with a concentrator and achieved an efficiency of 47.6%.[4,5] Despite the difference, c-Si solar cells dominate

the PV market (90% of the world PV cell production in 2008) because of scalability to modules and panels, as well as offering a good balance between cost and efficiency.[6]

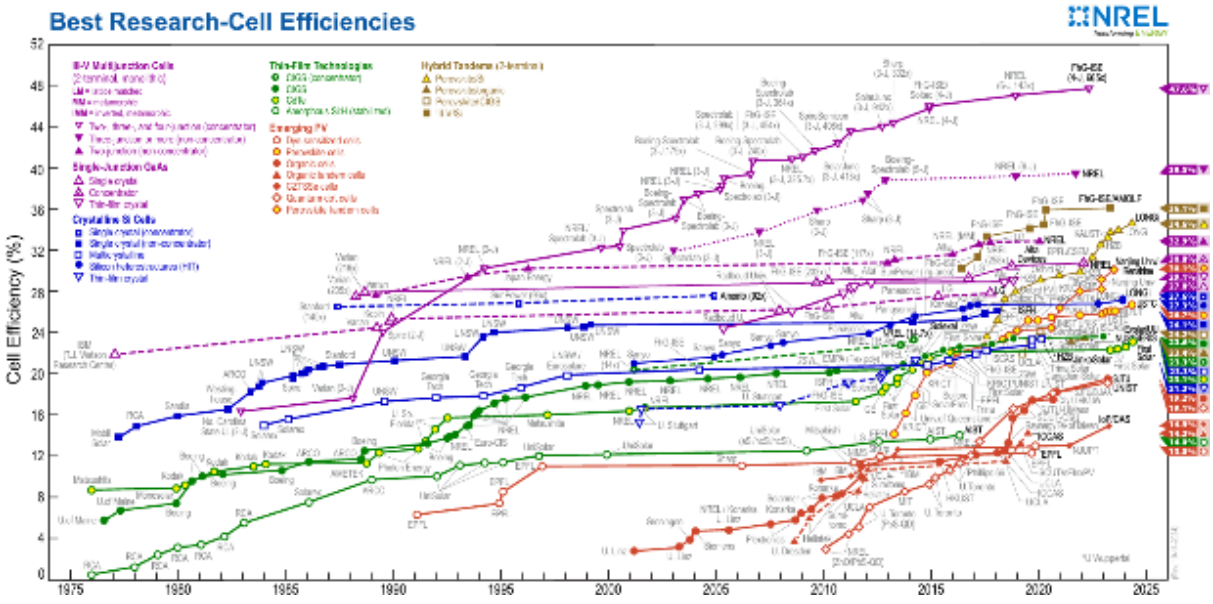

Figure 1. Chart by the National Renewable Energy Laboratory of highest confirmed conversion efficiencies of research solar cells from 1976 to present.

1.1.1 Silicon Solar Cells

As previously mentioned, c-Si solar cells are the preferred PV technology for large scale applications and can be divided into two types, mono- and polycrystalline silicon (mc-Si and pc-Si).[6] Between the two, solar cells made from mc-Si have a slight advantage over those made from pc-Si because defects in the grain boundaries can introduce energy levels that hinder charge mobility and therefore act as recombination sites.[7,8] Whether solar cells are made from mc-Si or pc-Si, the working principles are the same.

Silicon is a semiconductor material in which the energy gap between the valance band (VB) and conduction band (CB), the band gap (E_g), is approximately 1.1 eV; large enough to prevent the formation and separation of charges without external stimuli.[9,10] However, under illumination, photons supply enough energy to excite electrons in the VB

which allows them to cross the E_g into the CB through the photovoltaic effect. Crystalline silicon solar cells leverage this property by introducing impurities into the silicon lattice in a process known as doping. Positively doped silicon crystals, p-type, contain atoms with one less electron in their VB than silicon (i.e. boron or gallium), while negatively doped silicon crystals, n-type, contain atoms with one more electron in their VB than silicon (i.e. phosphorus or arsenic) (figure 2). At the interface of the p-n junction, the excess electrons in the n-type silicon recombine with the holes in the p-type silicon creating a depletion zone between the two layers. The negative and positive charges that accumulate in the p-type and n-type depletion regions, respectively, generate an internal electric field that prevents further diffusion of holes and electrons from the bulk material and facilitates charge separation in c-Si solar cells. Upon photoexcitation, the electric field mobilizes excited electrons and holes originating from the depletion zone toward the n-type and p-type layers, respectively. Electric current is generated as excited electrons in the n-type layer enter an external circuit and travel towards the p-type layer to recombine with the holes (figure 3).

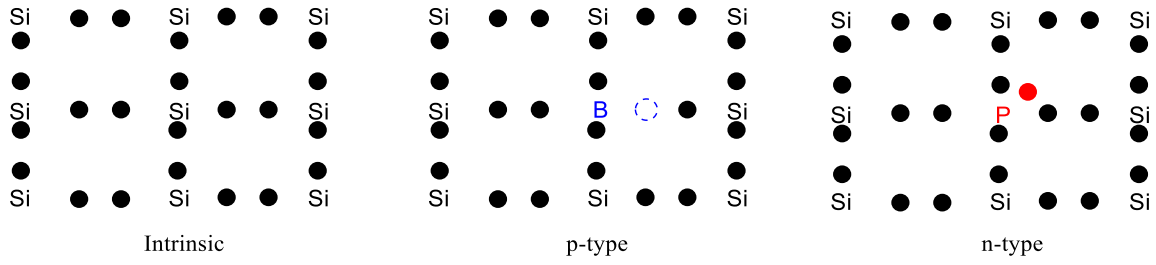

Figure 2. Intrinsic silicon lattice with four valence electrons (left), silicon lattice p-doped with trivalent boron (middle), and silicon lattice n-doped with pentavalent phosphorus (right).

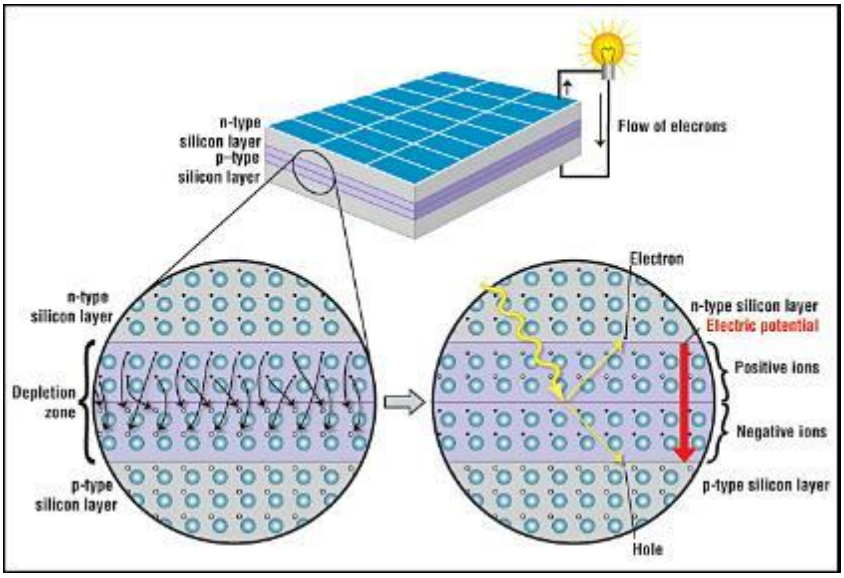

Figure 3. Schematic of working principle of c-Si solar cells with a p-n junction.

Despite their success and their balance between cost and efficiency in relation to other PV technologies, appeal is diminished as the requirement of high-purity silicon leaves the production cost of c-Si solar cells susceptible to market pressure.[6] Therefore, developing novel materials that are both cost-effective and efficient is at the crux of PV research.

1.1.2 Dye-Sensitized and Solid-State Dye Sensitized Solar Cells

Potential alternatives to c-Si solar cells are thin-film dye-sensitized (DSSCs) and solid-state dye sensitized solar cells (ssDSSCs); denoted as (ss)DSSCs when applicable to both. Compared to the higher efficiencies of c-Si based PVs, 27.6%, the efficiencies of DSSCs and ssDSSCs are significantly lower at 13.0% and 11.7%.[4,11] Regardless, (ss)DSSCs are attractive because improvement is possible as they have yet to reach their efficiency limit of 23.78% and 35-41% under one sun illumination and diffuse light conditions, respectively.[12] The ability to perform under low light conditions is significant for practical applications since the incident angle and intensity are variable throughout the day.[13] At intermediate angles, c-Si solar cells require antireflective layers to compete

with DSSCs (normalized efficiencies), adding an additional expense to solar cell production. DSSCs on the other hand, do not require this modification as they benefit from the increased optical path length that allows for greater light absorption. Since increasing light absorption is a viable strategy to increase the performance of any PV technology, (ss)DSSCs have an additional advantage of utilizing photosensitive dyes that can be tuned or modified to meet light absorption requirements and optimize energetic alignment with adjacent layers.[14]

Unlike c-Si solar cells, charge generation and separation are compartmentalized between three layers; a photoactive dye absorbs photons to generate electron-hole pairs (e^-/h^+), a metal-oxide semiconductor mobilizes electrons, and a redox mediator mobilizes holes to reduce the oxidized dye.[14] The concept of implementing a sensitizer to generate current was discovered in the 1960s through the application of organic dyes in electrochemical cells and was expanded upon in 1972 with the development of a chlorophyll-sensitized zinc oxide (ZnO) electrode.[15] In 1991, the architecture for modern DSSCs was established by O'Regan and Grätzel.[16] By using a high-surface area and wide band gap (E_g = 3.2 eV) semiconductor, anatase titanium dioxide (TiO_2), a trimeric ruthenium complex as a dye, $RuL_2(\mu\text{-}(CN)Ru(CN)L'_2)_2$ (L = 2,2'-bipyridine-4,4'-dicarboxylic acid and L'= 2,2'-bipyridine), and a liquid electrolyte, efficiencies of 7.1-7.9% and 12% were achieved under simulated and diffuse daylight, respectively.

A similar architecture is present in ssDSSCs; however, the liquid electrolyte is replaced by a solid hole transporting material (HTM) to mitigate efficiency loss due to leakage or evaporation. The most common electrolyte solutions used in DSSCs consist of an iodide/triiodide ($3I^-/I_3^-$) redox couple.[17] At the dye/electrolyte interface, iodide ions

reduce the dye molecules and are oxidized to triiodide in return, which are then reduced back to iodide at the counter electrode. The most common HTM used in ssDSSCs is 2,2',7,7'-tetrakis-(N, N-di-4 methoxyphenylamino)-9,9'-spirobifluorene (Spiro-MeOTAD) and serves the same purpose however it is significantly faster than the liquid electrolyte, pico- vs microseconds (ps vs μs).[11] This is attributed to direct hole transfer from the dye to the HTM, while electrolyte ions must diffuse through the liquid medium between the electrodes to undergo redox reactions. Nevertheless, DSSCs outperform ssDSSCs because of inferior TiO_2 penetration by the HTM.[18] This leaves deeply embedded dye molecules unable to be reduced and susceptible to recombination; however, this can be addressed by optimizing the thickness and/or deposition methods of the following layers: TiO_2, Dye, and HTM. Regardless of the redox mediator, the working principles are similar.

1.2 (ss)DSSCs Working Principles

A simple representation of the photon-to-current mechanism in (ss)DSSCs is depicted by the green arrows (1-3) in figure 4. Photosensitive dyes adsorbed onto the surface of TiO_2 absorb incident photons that excite electrons within their highest occupied molecular orbital (HOMO) to their lowest unoccupied molecular orbital (LUMO) (1). The dye LUMO is located at a higher energy level and possesses a lower redox potential (more negative) than the TiO_2 CB which facilitates interfacial charge injection (2), an ultrafast process that occurs in femto- to picoseconds (fs to ps).[19] The injected electrons diffuse through the TiO_2 lattice towards a fluorine doped tin oxide (FTO) glass substrate, enter an external circuit, and travel towards the counter electrode to generate current. This process is reproducible because the sensitizer's HOMO is

regenerated by either a liquid electrolyte (3) in DSSCS or a solid HTM (3') ssDSSCs. Because of energetic and physical proximity between the oxidized dye and HTM, regeneration of the HOMO occurs orders of magnitude faster in ssDSSCs (ps) than in DSSCs (µs). Moreover, the lower lying energy level of the HTM in comparison to the electrolyte results in overall higher open-circuit voltage (V_{oc}) in ssDSSCs. This mechanism described by the green arrows is of an ideal process in efficient (ss)DSSCs. In reality, electron mobility and efficiency are hindered by competing recombination processes that arise from defects within or at the interface of the (ss)DSSC's layers, arrows 4-6 in figure 4.

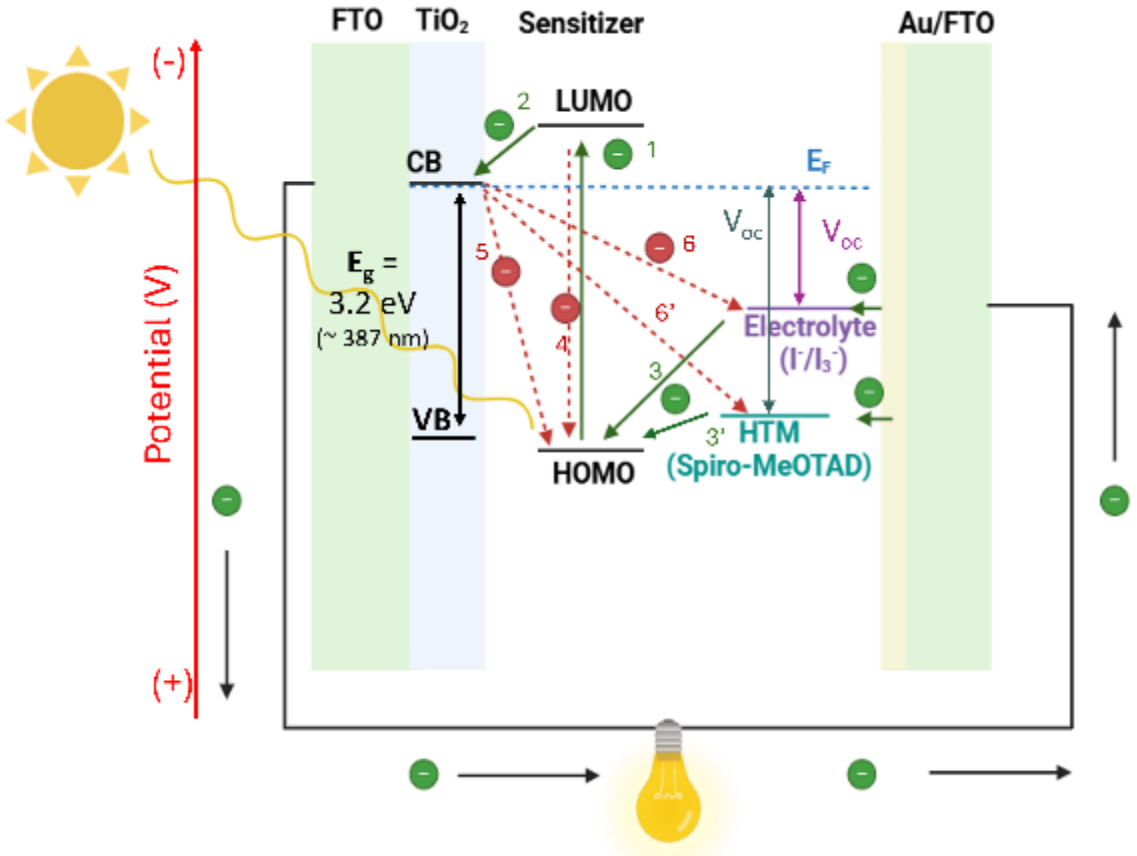

Figure 4. Schematic of (ss)DSSC working principles. Green arrows represent pathways that produce current (1-3), red arrows represent recombination pathways that hinder efficiency (4-6), and the blue arrow represents hole mobility.

1.2.1 Metal-oxide Semiconductor

There are a variety of metal-oxide semiconductors such as Nb_2O_5, ZnO, SnO_2, and NiO however, anatase TiO_2 is the most commonly used in high efficiency (ss)DSSCs.[11,14,15] The utility of TiO_2 semiconductors stem from their transparency to visible light, porosity, and suitable orbital overlap and alignment with adsorbed dyes.

Anatase titanium-dioxide's wide bandgap, $E_g \sim 3.2$ eV, is suitable for absorbing a portion of the UV spectrum ($\lambda \sim 387.5$ nm) however, approximately only 8% of incident light is comprised of UV radiation; the remaining 42.3% of visible and 49.4% of infrared (IR) radiation is either transmitted, scattered or weakly absorbed.[20,21] The transmitted radiation is meant to be absorbed by the dye monolayer. Moreover, the dye monolayer is greatly increased as the porosity of the metal-oxide layers typically increases the surface area by a factor of about 1000.[14] The increased dye loading and surface area benefit (ss)DSSC performance since dye molecules typically have low-absorption cross-sections; $\sigma_{N719} = 4.94\text{x}10^{-17}$ cm^2 and $6.4\text{x}10^{-17}$ cm^2 at 400 nm and 520 nm, respectively.[22,23]

Stable dye adsorption onto the TiO_2 surface is facilitated by anchoring groups on the sensitizer such as pyridines and phosphonic acids, but most prominent, carboxylic acids in transition metal complexes such as Ru^{II}-polypyridyl dyes.[24,25] In addition to dye adsorption, the electron withdrawing nature of these carboxylic acid moieties creates an electron accepting environment (LUMO) that is spatially and energetically close to the TiO_2 CB; charge injection is aided by this proximity. Moreover, the binding modes between carboxylic acids and TiO_2 depicted in figure 5 greatly influence charge injection and adsorption stability; these binding modes are monodentate ester, bidentate bridging,

monodentate binding, or bidentate chelating.[24] Between the four, bidentate chelating and bridging exhibit the most stability.[14,25]

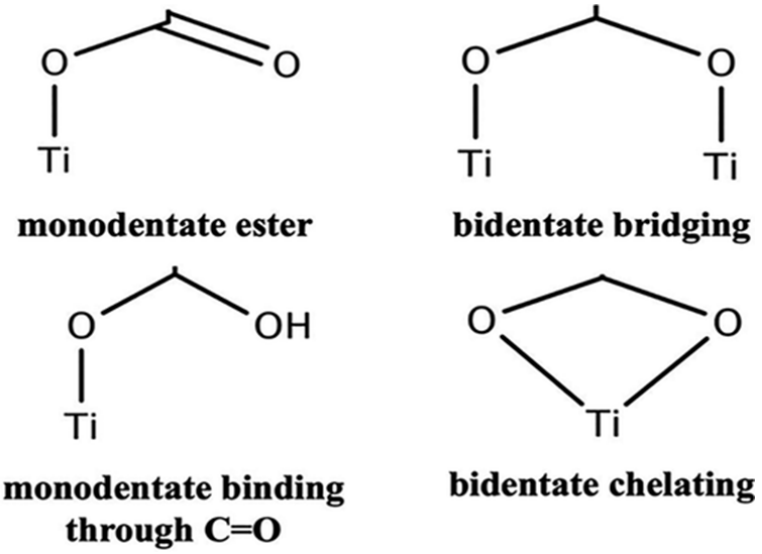

Figure 5. Different binding modes adopted by carboxylic acid/carboxylate groups anchored onto TiO_2.[24]

The successful pairing of TiO_2 and carboxylic acid anchor groups is due to the favorable overlap between Ti^{IV} 3d orbitals and the anchor's orbitals depicted in figure 6A.[26] This co-planar configuration of the ester binding mode and the ligand π-system is speculated to occur only in the excited state (HOMO to LUMO). Unfavorable steric interactions in the ground state offsets the ester plane by 10-15^{o} relative to the rest of the dye ligand (figure 6B) and electron injection suffers. The relationship between orbital overlap and charge injection emphasizes the preference for TiO_2 semiconductors in (ss)DSSCs. Additionally, the applicability of metal-oxides such as SnO_2 in which the Sn s orbitals interact poorly with the anchor group orbitals (figure 6C) suggests that appropriate alignment of the orbital energy levels is enough to promote electron injection, albeit not as efficiently. Therefore, efficient TiO_2 (ss)DSSCs require Ru^{II}-polypyridyl

dyes with carboxylic acid anchor groups whose LUMOs are close but higher in energy than the TiO_2 CB (~ -0.5 V vs NHE).[19,27]

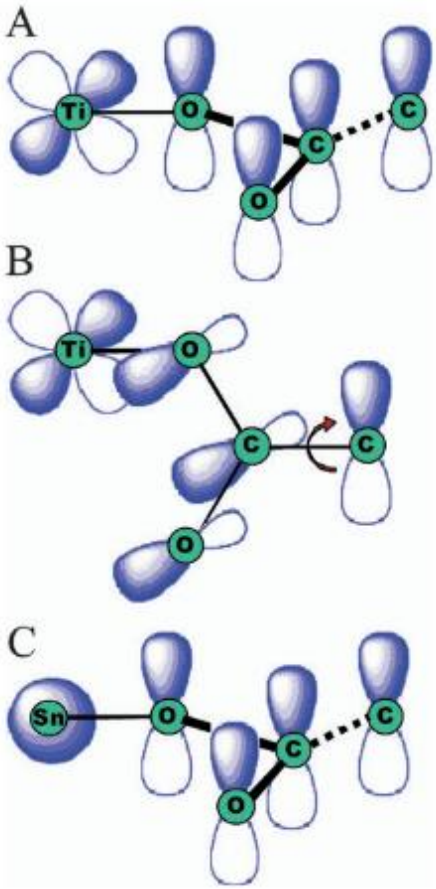

Figure 6. A) Favorable orbital overlaps between excited dye orbitals and Ti^{IV} 3d orbitals in a monodentate ester binding mode. B) Unfavorable orbital interactions between the anchor ground state and the Ti^{IV} 3d orbitals. C) Poor orbital mixing between the anchor orbitals and Sn s orbital.

1.2.2 Sensitizer

The following properties should be present in efficient sensitizers: anchor groups that provide adsorption stability and aid in charge injection, higher oxidation potential than the redox mediator for efficient dye regeneration, a more cathodic LUMO than the TiO_2 CB for charge injection, intense light absorption ($\varepsilon \sim 10^4$ M^{-1} cm^{-1}) to promote thin TiO_2/dye films, and a broad absorption spectra that encompasses that extends beyond

visible light (~400-700 nm) to about 940 nm.[21,28] The Ru^{II}-polypyridyl complex sensitizers depicted in figure 7 are the most commonly used in (ss)DSSCs because they fulfill these requirements. For example, the most studied of these complexes, N719, exhibits intense absorption peaks at 310 (π-π*) and 530 nm (HOMO to LUMO) and possesses a LUMO that is 200 mV more cathodic than the TiO_2 CB (vs NHE).[29-31] Chapter 2 will discuss the HOMO to LUMO excitation process as well as strategies to address any limitations of the listed requirements.

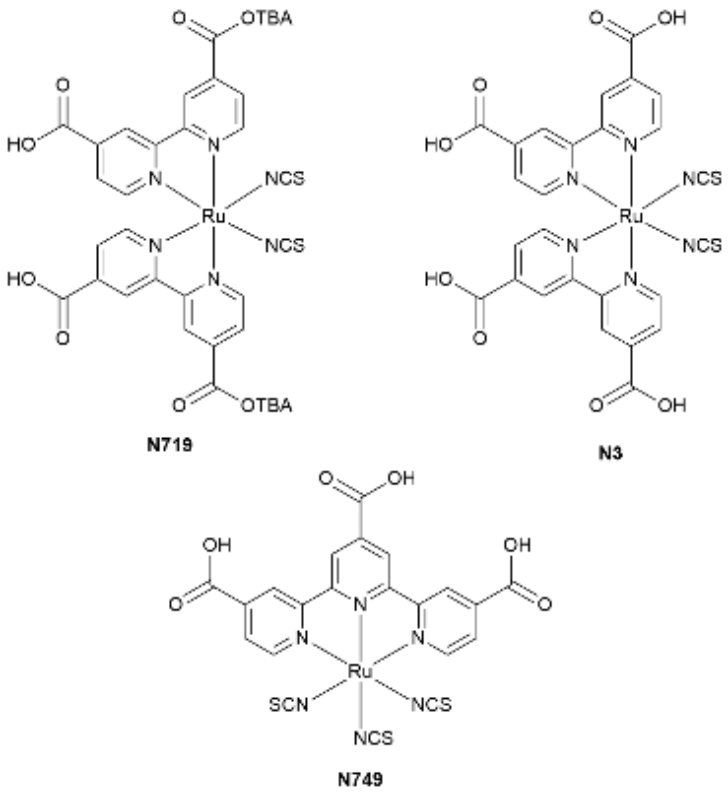

Figure 7. The most commonly used Ru^{II}-polypyridyl sensitizers used in efficient (ss)DSSCs; N719, N3, and N749.

1.2.3 Hole Transporting Materials

In ssDSSCs the most prominent hole transporting material (HTM) is 2,2',7,7'-tertakis(N,N-di-*p*-methoxyphenyl-amine)9,9'-spirobifuorine (spiro-MeOTAD) depicted in figure 8. Its ability to mobilize holes away from the oxidized dye is attributed to less

positive oxidation potential (~ 0.76 V vs NHE) than the dye HOMO.[32] Additionally, the HTM further enhances ssDSSC performance through the inclusion of additives that modulate the TiO_2 CB such as LiTFSI and 4-tert-butyl-pyridine(tBP); Li^+ ions shift the CB to more positive potentials enhancing charge injection, and t-BP shifts the CB to more negative potentials increasing the V_{oc}.[33] Other inclusions include Co (III) salts such as FK102, FK209 and FK269 that serve to enhance the HTM hole conductivity by oxidizing the spiro-MeOTAD.[34]

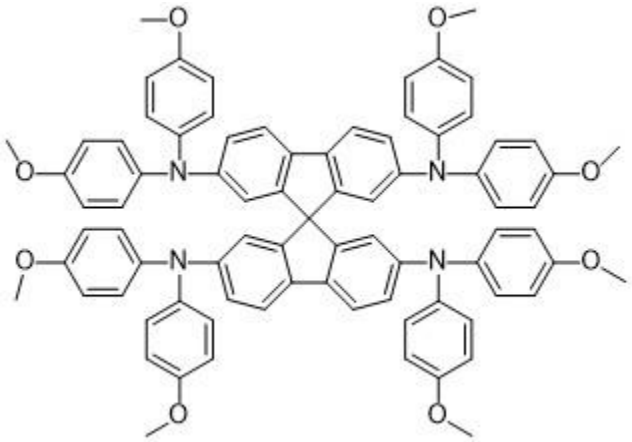

Figure 8. Structure of spiro-MeOTAD.

1.3 Power Conversion Efficiency

Power conversion efficiency (PCE) describes how well a solar cell converts incident photons into usable electrical energy. PCE can be determined via linear sweep voltammetry; by illuminating a solar cell while its current is measured against a sweeping voltage, a current-voltage (IV) curve is obtained. The IV curves are usually standardized and converted to current density-voltage (JV) curves by dividing the current by the active area of the solar cell. Figure 9 depicts a typical JV curve and the parameters used to determine the solar cell's efficiency.

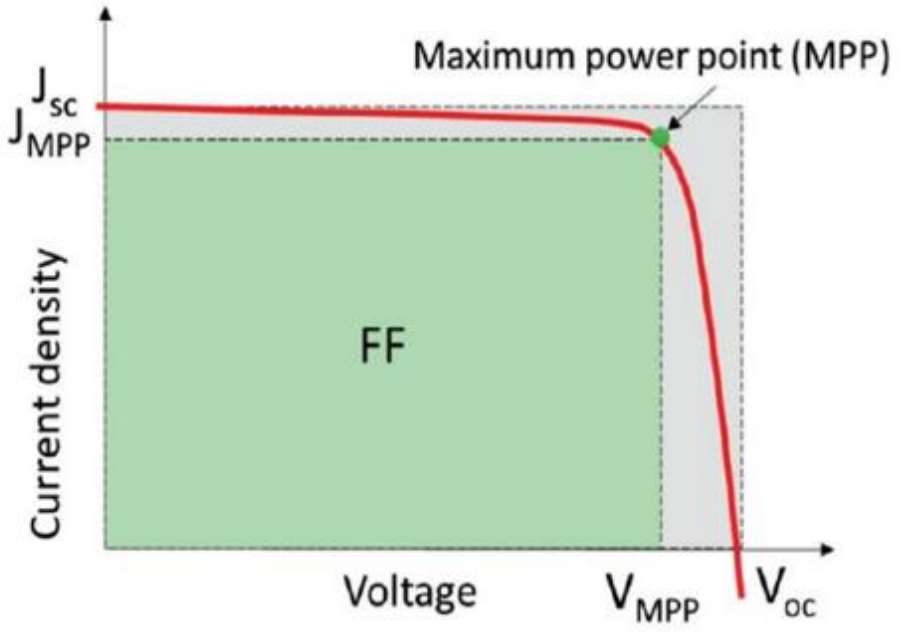

Figure 9. Ideal JV curve shape and parameters related to (ss)DSSC quality and performance.

The open-circuit voltage (V_{oc}) represents the energy difference between the Fermi level (E_F) and the redox potential of the redox mediator. The E_F itself is dependent on the number of electrons in the TiO_2 CB. At the open-circuit condition, electrons are unable to enter the external circuit and accumulate in the CB. This raises the E_F close to the CB and the maximum voltage the cell can generate, the V_{oc}, is achieved (figure 4). A large V_{oc} is a good indicator of favorable orbital energy alignment between the dye LUMO and TiO_2 CB. The short-circuit current density (J_{sc}) is the maximum current the solar cell can produce. At this point, electrons are continuously being transported into the external circuit preventing them from accumulating in the CB and therefore the voltage is 0. The J_{sc} is closely related to efficient light absorption and charge injections. The solar cell produces its highest electrical power at the max power point (MPP) and J_{MPP} and V_{MPP} are

the corresponding current density and voltage. These parameters are used to determine the fill factor (FF) and PCE via equations 1 and 2, respectively.

$$FF = \frac{V_{MPP} \bullet J_{MPP}}{V_{oc} \bullet J_{sc}} \quad (1)$$

$$PCE = \frac{V_{oc} \bullet J_{sc} \bullet FF}{P_{in}} \bullet 100\% \quad (2)$$

The FF is the ratio of the maximum power to the theoretical maximum power and describes how well the solar cell is performing to its theoretical maximum. The PCE of a solar cell is calculated by equation 2 in which P_{in} is the input power. Substituting FF by equation 1 simplifies equation 2 into the maximum power output over the power input.

1.3.1 ssDSSC Characterization

Injected electrons in the TiO_2 can either diffuse towards the external circuit and contribute to power production or recombine with the oxidized dye and/or the redox mediator and efficiency is lost. Defects in the (ss)DSSC architecture may delay dye regeneration and hole mobility, and electron diffusion through TiO_2 towards the FTO glass is a relatively slow process, therefore quantifying the electron lifetime ($\boldsymbol{\tau_n}$) in the TiO_2 CB is crucial for understanding (ss)DSSC performance, quality and recombination kinetics.

Zaban et al. described a method for determining the $\boldsymbol{\tau_n}$ of operational (ss)DSSCs as a function of V_{oc} via the open-circuit voltage-decay (OCVD) technique.[35] By illuminating (ss)DSSCs at the open-circuit condition, current does not flow through the device and free electrons accumulate in the TiO_2 CB until the (ss)DSSC achieves a steady state; a balance between charge injection/recombination, and trapping/detrapping. At the steady state, the increase of electrons raises the Fermi level close to the TiO_2 CB edge and the cell's upper limit V_{oc} is achieved. The OCVD measurements are obtained by

shutting off the illumination allowing the injected electrons to undergo recombination that is observed as the decrease in V_{oc} over time (figure 10a).

The rate of recombination **U** (electrons • cm^{-3} • s^{-1}) is described as $\mathbf{U = k_r n^{\beta}}$ where $\mathbf{k_r}$ is the recombination constant (units depend on **β**), **n** is the electron density in the CB (electrons • cm^{-3}), and **β** is an effective recombination order whose value corresponds to the types of recombination mechanisms present in (ss)DSSCs and describes how a wide range of internal conditions affect the lifetime $\boldsymbol{\tau_n}$. The OCVD curves in figure 10a describe the dependence of the steady-state and rate of recombination **U** on the electron density **n**; that is, the decay curves with larger initial V_{oc}'s as a result of increased electron density in the CB, due to more intense illumination, have steeper decays (faster recombination). On the other hand, the decay curves with lower initial V_{oc}'s as a result of decreased light intensity undergo shallower decays (slower recombination). A possible explanation for this behavior is the relative presence of trap states in relation to the number of free electrons in the CB. Applying equation 3 to the OCVD measurement to derive figure 10b provides a clearer description of this behavior; electron lifetimes $\boldsymbol{\tau_n}$ increase as V_{oc}'s decreases. This is true in isolation however, because of the power-law nature of the recombination rate, the electron density **n** influence on the rate of recombination **U** is dependent on the recombination order **β**. Since the electron lifetime can be described as $\boldsymbol{\tau_n = n/U}$, simplification describes the effects of the recombination order on lifetime, $\boldsymbol{\tau_n = 1/(k_r n^{\beta-1})}$. The recombination order **β** is a significant because it provides insight into the dominant recombination mechanism in the (ss)DSSC (figure 10c) and is obtained by applying equation 4 to figure 10b.

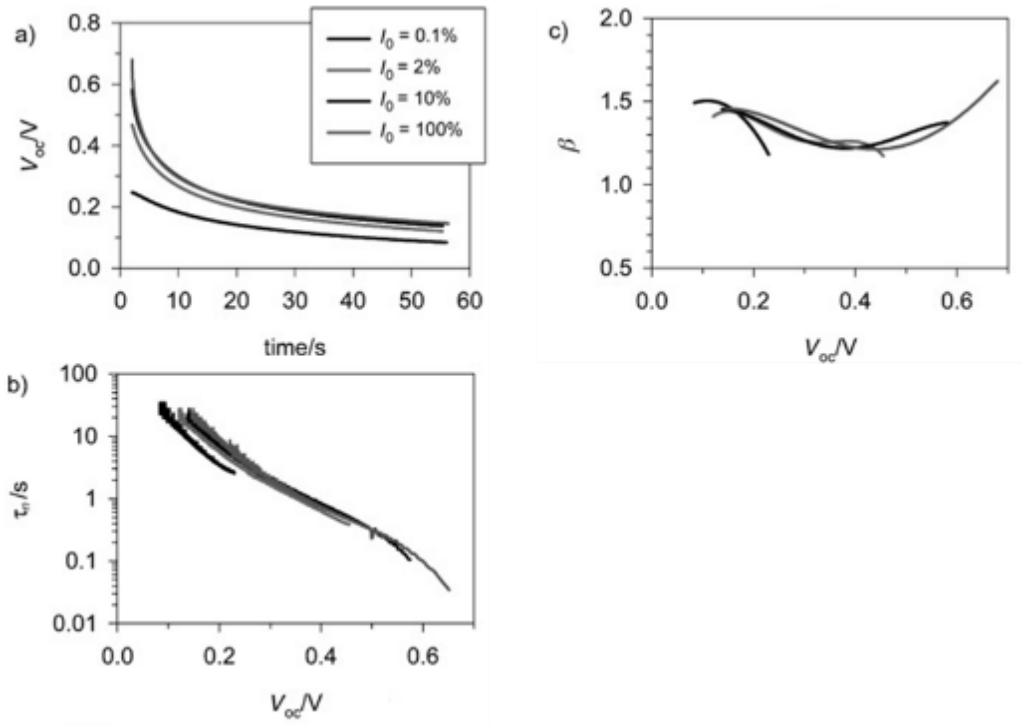

Figure 10. a) OCVD measurements, b) electron lifetime (equation 3), and c) recombination order (equation 4) of DSSCs determined at different light intensities.[35]

$$\tau_n = -\frac{k_B T}{e}\left(\frac{dV_{oc}}{dt}\right)^{-1} \quad (3)$$

$$\beta = 1 + \frac{k_B T}{e}\frac{d\ln\tau_n^{-1}}{dV_{oc}} \quad (4)$$

- Boltzmann constant (k_B) = 1.380649 x 10^{-23} J/K
- Temperature (T) in kelvin
- Elementary charge I = 1.60217663 x 10^{-19} C

CHAPTER 2

RUTHENIUM POLYPYRIDYL COMPLEXES AS SENSITZERS

2.1 Metal-to-Ligand Charge Transfer

Most dyes used in (ss)DSSCs are based on Ru^{II}-polypyridyl complexes that mainly adopt an octahedral geometry (figure 7). The octahedral geometry gives rise to a specific molecular orbital arrangement that dictates the initial HOMO to LUMO excitation process. For simplicity, figure 11 depicts a simple molecular orbital diagram of the homoleptic complex, $[Ru(bpy)_3]^{2+}$ (bpy is 2,2'-bipyridine), assuming O_h symmetry by only considering the lone pairs on the nitrogen and neglecting the ∠N-Ru-N angle ≠ 90°. In reality $[Ru(bpy)_3]^{2+}$ has D_3 symmetry. Ruthenium's one s, three p and two d (dz^2 and dx^2-y^2) atomic orbitals form six σ-bonds with the lone pairs of the surrounding ligands.[28] This is because the ligands p-orbitals have irreducible representations A_{1g}, T_{1u} and E_g that correspond to the ruthenium's s, p and d-orbitals respectively. The remaining ruthenium d-orbitals, d_{xy}, d_{xz} and d_{yz}, adopt T_{2g} representations that are unable to form σ-bonds with the ligands, however, they are able to participate in π-bonding that give rise to the HOMO and LUMO molecular orbitals. The energetic arrangement of the π-molecular orbitals is influenced by the π-donor or π-acceptor nature of the ligands. In the case of $[Ru(bpy)_3]^{2+}$, interactions between the remaining σ-nonbonding d orbitals of the ruthenium (t_{2g}) and π orbitals (t_{2g}) generates bonding (t_{2g}) and antibonding (t_{2g}*) molecular orbitals (figure 12). Pyridines are π-donating ligand and thus fill the bonding t_{2g} orbitals. The antibonding t_{2g}* orbitals are fille with six Ru^{II} electrons to generate the HOMO that is mainly localized on the ruthenium. The LUMO is comprised of the empty π* orbitals that are mainly localized on the ligands. Therefore, the absorption and

excitation from the HOMO to the LUMO is a metal-to-ligand charge transfer (MLCT) from the ruthenium t_{2g}* to the ligand π*.

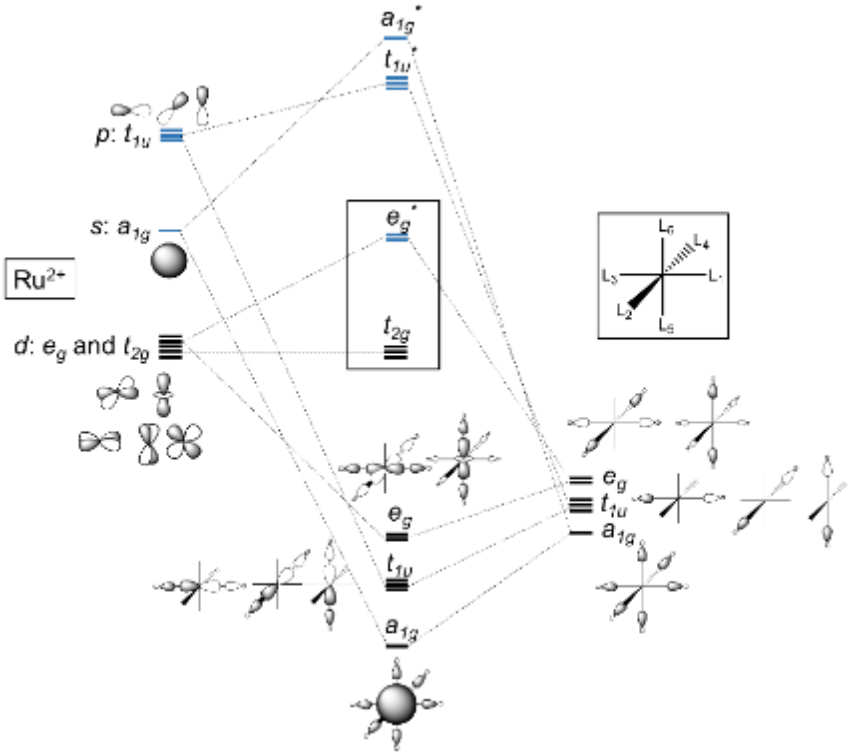

Figure 11. σ-bonding molecular orbital diagram of an octahedral Ru^{II} complex. The black and blue bars represent full and empty orbitals, respectively.[28]

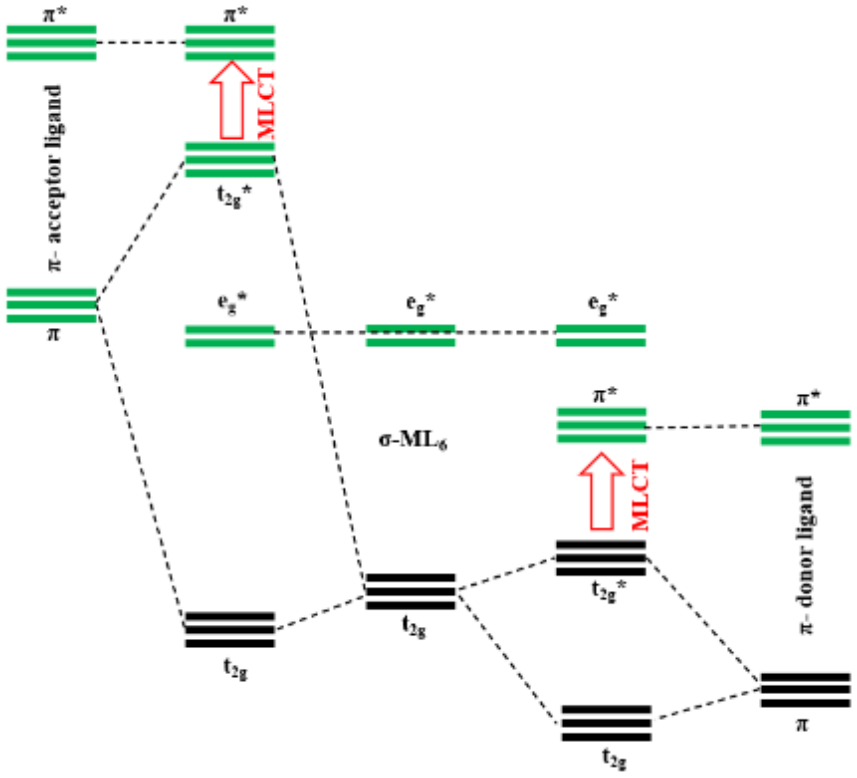

Figure 12. Molecular orbital diagram of π interactions between a metal and π-accepting and π-donating ligands.

The advantage of using Ru^{II}-polypyridyl sensitizers to absorb light is derived from facile tunability to the complex that allows for control over the MLCT. The effect of π-donor (D) and π-acceptor (A) substituents on the t_{2g} and π* orbitals of $[Ru(bpy)_3]^{2+}$ are depicted in figure 13.[28] Simply put, π-donor ligands have a greater effect on destabilizing the metal t_{2g}* while weaker π-donators/π-acceptors have a greater effect on stabilizing the ligand π*. Although different complexes will differ in their orbital splitting as a result of their ligand systems, the qualitative Interactions in figure 13 are good representations of how ligands and/or substituents affect the MLCT.

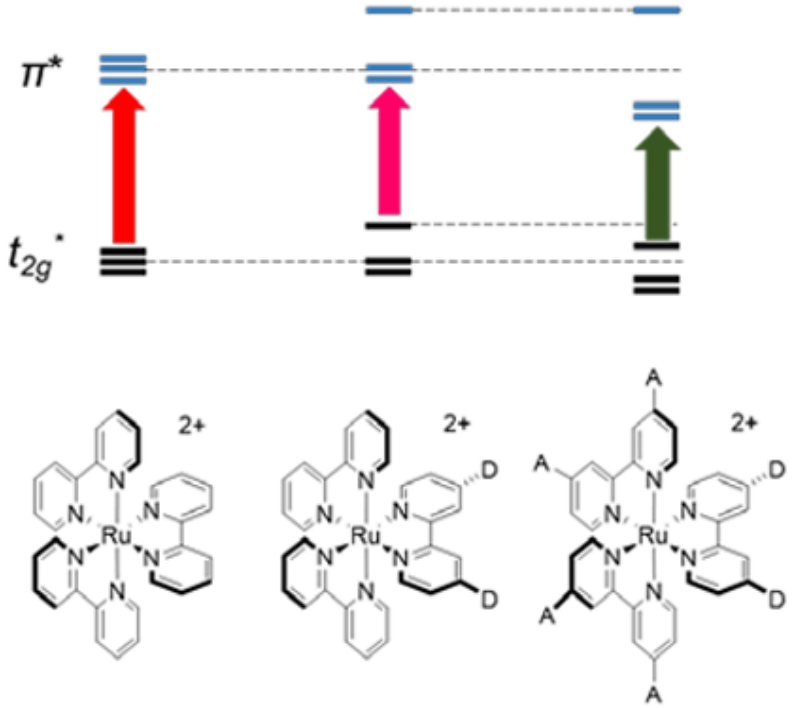

Figure 13. The effect of π-donor (D) and π-acceptor (A) substituents on the MLCT orbitals of Ru^{II}-polypyridyl dyes.

2.1.1 Dye Limitations and Strategies to Enhance Light Harvesting

Efficient light absorption and electron injection requires a monolayer of dye to be adsorbed onto the TiO_2 surface (figure 14, left). This limits TiO_2 dye loading, results in insufficient light absorption and consequently diminishes (ss)DSSC PCE. Dye multilayers are not a viable solution as the subsequent dye layers after the TiO_2/dye interface are insulated by the first layer, hindering electron mobility.[36] Increasing the surface area through thicker TiO_2 layers is also an ineffective strategy to improve absorption as the longer electron diffusion path increases series resistance and hinders electron mobility (figure 14, right). Increasing the light harvesting capabilities of the dye is a more viable strategy to improve (ss)DSSC performance and is possible through the

tunability of the Ru^{II}-polypyridyl dye structure and therefore the MLCT orbitals (figure 13).

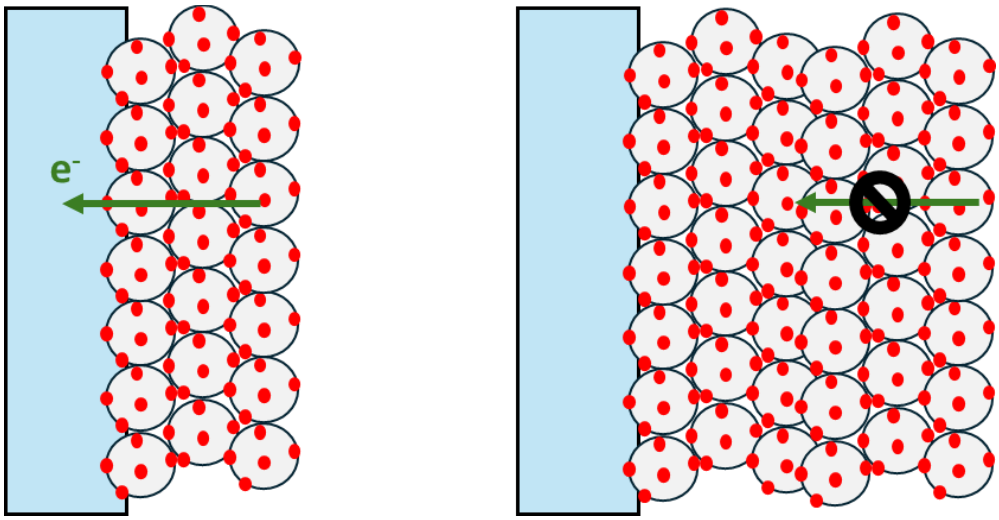

Figure 14. Monolayer of dye molecules on TiO_2. Depiction of efficient electron diffusion through a thin TiO_2 layer (left). Depiction of increased dye loading but hindered electron diffusion as a result of thicker TiO_2 layers (right).

Yu et al. observed a trend of increasing DSSC PCE through the implementation of three Ru(dcbpy)(L)$(NCS)_2$ based dyes in which dcbpy is 4,4'-dicarboxylic acid-2,2'-bipyridine and L is a 2,2'-bipyridine (bpy) ancillary ligand functionalized with increasingly π-conjugated moieties.[37] DSSCs sensitized with **Z907** (L = 4,4'-dinonyl-2,2'-bipyridine), **C103** (L = 4,4'-bis(5-hexyl-3,4-ethylenedioxythiophene)-2,2'-bipyridine), and **C107** (L = 4,4'-bis(5-octyl-3,4-ethylenedioxythiophene)-2,2'-bipyridine), depicted in figure 15, obtained PCEs of 9.1, 10.4, and 10.7%, respectively. The increasing molar extinction coefficients and red-shifts of the MLCT bands of dyes **C103** ($20.5x10^3$ M^{-1} cm^{-1} at 550 nm) and **C107** ($27.4x10^3$ M^{-1} cm^{-1} at 559 nm), in comparison to **Z907** ($12.2x10^3$ M^{-1} cm^{-1} at 521 nm), were indicative of the increased PCEs being attributed to enhanced light harvesting brought on by the electron-rich 3,4-ethylenedioxythiophene moieties. The JV-parameters reflected enhanced light harvesting

and PCEs through improvements in the J_{sc}, 16.46, 18.35, and 19.18 mA cm^{-2} for DSSCs sensitized with **Z907**, **Cl03**, and **C107**, respectively. However, the increasing lateral diameter of the dyes diminished the surface coverage of the TiO_2 layer (**Z907**: 9.58x10^{-11} mol cm^{-2}; **C103**: 6.64x10^{-11} mol cm^{-2}; **C107**: 3.38x10^{-11} mol cm^{-2}) and consequently the V_{oc} (**Z907**: 769 mV; **C103**: 760 mV; **C107**: 739 mV). The relationship between decreasing surface coverage and V_{oc} was attributed to faster charge recombination at the TiO_2/electrolyte interface due to more electron-trapping states at "exposed" TiO_2. This work highlights potential trade-off between enhanced light-harvesting and surface coverage.

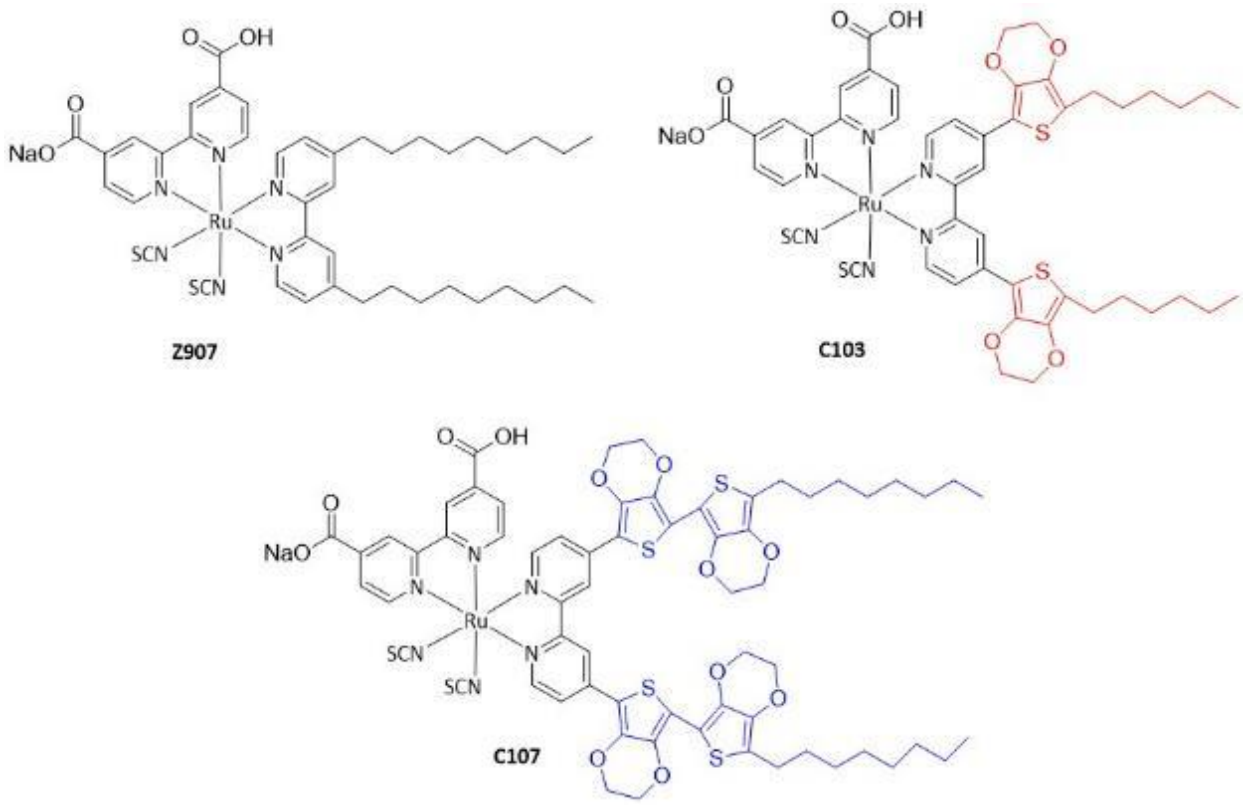

Figure 15. Ruthenium-polypyridyl dyes with increasing π-conjugation, **Z907** < **C103** < **C107**.

Within the same strategic realm, increasing the probability of MLCT by utilizing multinuclear complexes is another strategy to improve the light-harvesting abilities of

Ru^{II}-polypyridyl dyes. Amadelli et al. designed a trinuclear complex in which two antenna Ru-bipyridine chromophores were cyano-bridged to a carboxylate functionalized Ru-bipyridine complex, $[Ru(bpy)_2(CN)_2]_2Ru(bpy(COO)_2)_2^{2-}$ ($bpy(COO)_2^{2-}$ = 4,4'-dicarboxyl-2,2'-bipyridine) (figure 16).[36] In comparison to a mononuclear complex, $Ru(bpy(COO)_2)_3^{4-}$, the trinuclear complex exhibited high (420 nm) and low (526 nm) energy MLCT bands in its absorption spectrum corresponding to the antenna and central complexes, respectively (figure_a). The low energy MLCT bands of the central complex can be attributed to relatively more energetic t_{2g} orbitals as a result of the weak π-acceptor properties of the N-bonded CN bridge in addition to the carboxylate stabilized π*-orbitals (LUMO). Conversely, the stabilized t_{2g} as a result of the strong π-acceptor character of the C-bonded CN bridge, as well as the relatively destabilized LUMO, a result of the absence of an electron withdrawing moiety, gave rise to the higher energy MLCT band. These assignments were corroborated via cyclic voltammetry (CV) in which the oxidation potential of the center complex ($E_{1/2}^{ox}$ = 0.54 V vs SCE) was cathodically shifted relative to the antenna complex oxidation potential ($E_{1/2}^{ox}$ = 1.24 and 1.58 V vs SCE); the peak separation of the antenna $E_{1/2}^{ox}$ was attributed to metal-to-metal coupling across the CN bridge.

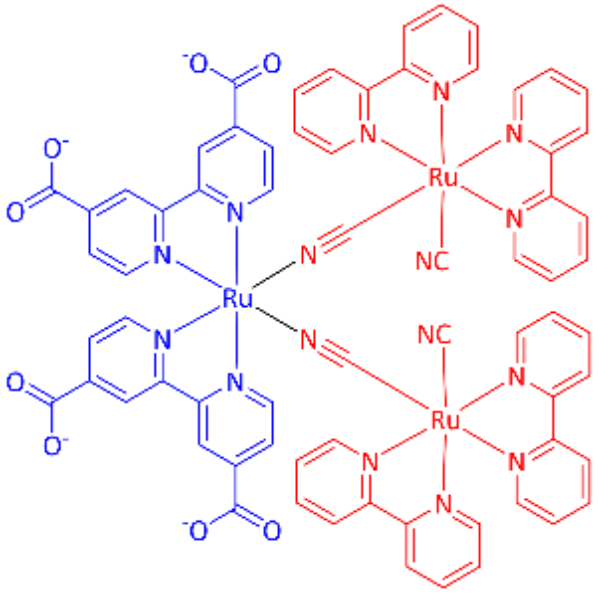

Figure 16. Trinculear complex, $[Ru(bpy)_2(CN)_2]_2Ru(bpy(COO)_2)_2^{2-}$, designed to increase light absorption through antenna complexes (red).

The trinuclear complex was designed to absorb higher energy photons through its antenna and funnel the excited electrons towards the carboxylate functionalized central complex where they undergo charge injection into the TiO_2. This mechanism is elucidated by figure 17a-d. Identical absorption (figure 17a) and excitation (figure 17b) spectra, along with the single emission band at 760 nm (figure 17b), strongly indicate intramolecular charge transfer from the antenna to the central complex. This charge transfer mechanism is depicted in figure 17c; excited electrons in the antenna undergo intersystem crossing (ISC) from the singlet (^{1}MLCT) to triplet (^{3}MLCT) excited states, followed by intramolecular charge transfer to the ^{3}MLCT state of the central complex. The photocurrent spectrum (figure 17d) of TiO_2 sensitized with the trinuclear complex strongly resembles the absorption spectrum (figure 17a) indicating efficient photon to current conversion of all absorbed photons, followed by charge injection through the central complex.

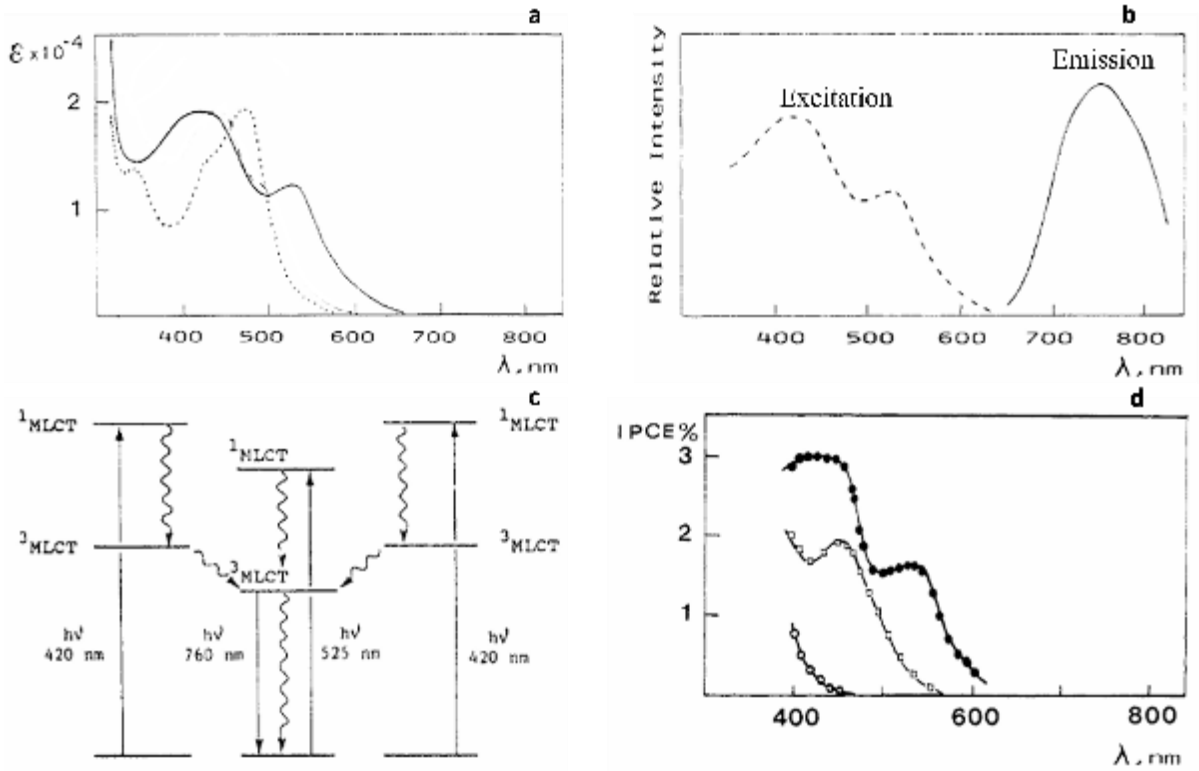

Figure 17. (a) Absorption spectra of mononuclear complex, $Ru(bpy(COO)_2)_3^{4-}$ (dotted line), and trinuclear complex, $[Ru(bpy)_2(CN)_2]_2Ru(bpy(COO)_2)_2^{2-}$ (solid line); (b) excitation and emission spectra of the trinuclear complex; (c) relative energy diagram and charge transfer mechanism; (d) photocurrent spectra of bare TiO_2 (circles), TiO_2 sensitized with the trinuclear complex (filled circle), and TiO_2 sensitized with the mononuclear complex (squares).

2.2 Goals

The goal of this research is to utilize the previously mentioned strategies and apply a highly conjugated, multinuclear, linear complex comprised of Ru^{II} and 1,4-di([2,2':6',2''-terpyridin]-4'-yl)benzene (tpy-ph-tpy or L) as sensitizers in (ss)DSSCs. In works by Vaduvescu and Potvin, comparisons of mono-, di-, and trinuclear ruthenium complexes show red-shifts and increased ε of the MLCT transitions as the number of Ru-L units increased.[38,39] This was explained as each additional unit having an electron withdrawing effect on the complex. In the mononuclear complex **1** [ttpy-Ru-ttpy](2PF_6^-), ttpy = 4'-p-tolyl-2,2':6',2''-terpyridine (figure 18), exchanging one ttpy ligand with L (**2**

[ttpy-Ru-L](2PF_6^-)) red-shifted and increased the extinction coefficient of the MLCT (ε) from 490 nm (1.55x10^4 M^{-1} cm^{-1}) to 496 nm (3.27x10^4 M^{-1} cm^{-1}). This trend continued for complexes **3** [ttpy-Ru-L-Ru-ttpy](4PF_6^-) (502 nm, 5.98x10^4 M^{-1} cm^{-1}) and **4** [ttpy-Ru-L-Ru-L-Ru-ttpy](6PF_6^-) (504 nm, 7.33x10^4 M^{-1} cm^{-1}). The red shifts in the MLCT transitions correspond to stabilization of the π* orbitals as demonstrated by the CV; values listed in table 1. The E_{ox} of Ru^{II} of complexes **1**-**4** (1.25- 1.27 V vs SCE) were unaffected by the increasing length of the complexes, indicating there is no metal-to-metal coupling, localized oxidation at each metal. Complexes with more Ru-L units experienced shifts of the first E_{red} to more positive potentials (-1.24- -1.03 V vs SCE), demonstrating reduction occurs at the L ligands.

The advantages of using such a complex are as follows: the high extinction coefficient and bathochromic shifts allow for increased light harvesting at longer wavelengths, multiple metals increase absorption sites for MLCT to occur while maintaining the monolayer requirement, rigidity may facilitate direct charge transport, and longitudinal growth may benefit dye loading.

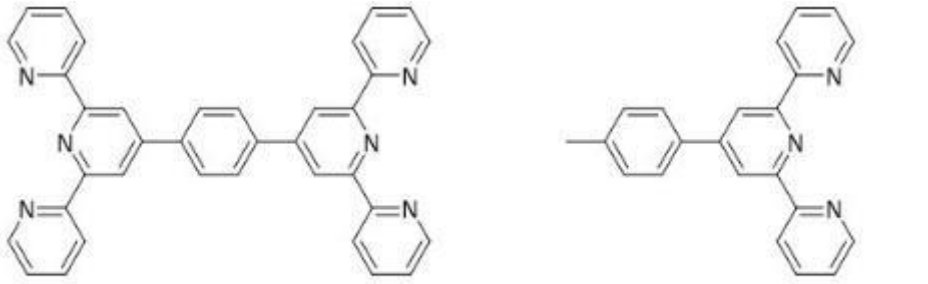

Figure 18. Ligands used in the synthesis of rigid, multinuclear, linear ruthenium complexes for sensitizer applications.

Table 1. Absorption and electrochemical data of linear ruthenium sensitizers.

Complex	**MLCT λ_{max} (nm) (ε (10^4 M^{-1} cm^{-1}))**	**E_{ox} (V vs. SCE)**	**E_{red} (V vs. SCE)**
1. [ttpy-Ru-ttpy]($2PF_6^-$)	490 (1.55)	1.25	-1.24, -1.42
2. [ttpy-Ru-L]($2PF_6^-$)	496 (3.27)	1.27	-1.18, -1.42
3. [ttpy-Ru-L-Ru-ttpy]($4PF_6^-$)	502 (5.98)	1.27	-1.18, -1.45
4. [ttpy-Ru-L-Ru-L-Ru-ttpy]($6PF_6^-$)	504 (7.33)	1.27	-1.03, -1.23

CHAPTER 3

MOLECULAR WIRES SYNTHESIS AND SSDSSC FABRICATION

3.1 Synthesis of $[Ru^{II}\text{-tpy-ph-tpy}]_n(2X)_n$

$[Ru^{II}\text{-tpy-ph-tpy}]_n(2Cl^-)_n$ was synthesized by following established methods.[40] Equimolar amounts of tetrakis(dimethylsulfoxide) dichlororuthenium (II) ($Ru(DMSO)_4Cl_2$) and 1,4-di([2,2':6',2''-terpyridin]-4'-yl) benzene (tpy-ph-tpy) were added and sealed in a two neck round bottom flask equipped with a rubber septum and a condenser with a Schlenk line adaptor (figure 19). Tubing was used to connect the adaptor to a Schlenk line that was used to evacuate air (5 min) from the round bottom flask and back fill it with N_2 gas (5 min). Three cycles were performed to ensure inert conditions for the reaction; each cycle consisted of one evac and one backfill step. After three cycles the reaction vessel was flushed with N_2 (argon in the original procedures) and anhydrous ethylene glycol was syringed into the round bottom flask through the rubber septum (1 mL/1 mg tpy-ph-tpy). Under vigorous stirring, the mixture was refluxed at 145-150 ^oC for 24 h. The resulting $[Ru^{II}\text{-tpy-ph-tpy}]_n(2Cl^-)_n$ was precipitated with tetrahydrofuran (THF), filtered and washed three times with THF, and dried under reduced pressure overnight. $[Ru^{II}\text{-tpy-ph-tpy}]_n(2PF_6^-)_n$ was obtained by treating $[Ru^{II}\text{-tpy-ph-tpy}]_n(2Cl^-)_n$ with excess ammonium hexafluorophosphate (NH_4PF_6). The precipitate was then filtered, washed with methanol, and dried under reduced pressure overnight. The reaction scheme for the synthesis of $[Ru^{II}\text{-tpy-ph-tpy}]_n(2Cl^-)_n$ is depicted in figure 20.

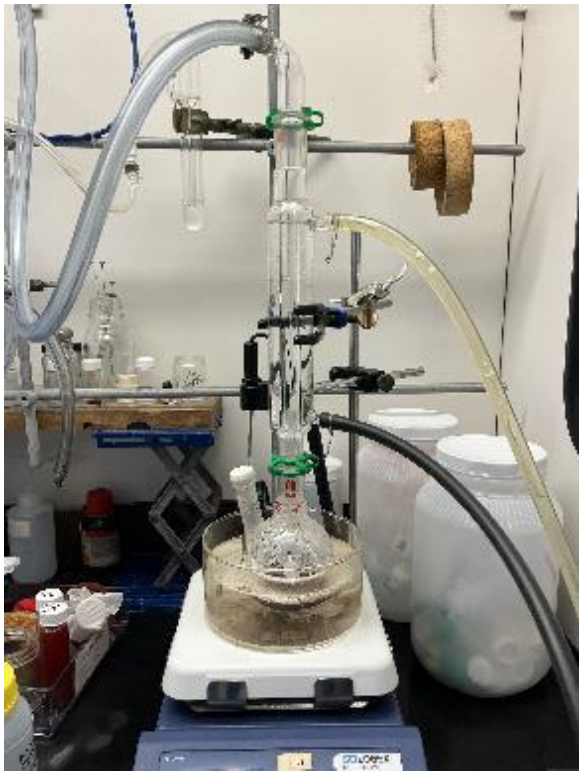

Figure 19. Reflux of $[Ru^{II}\text{-tpy-ph-tpy}]_n(2Cl^-)_n$.

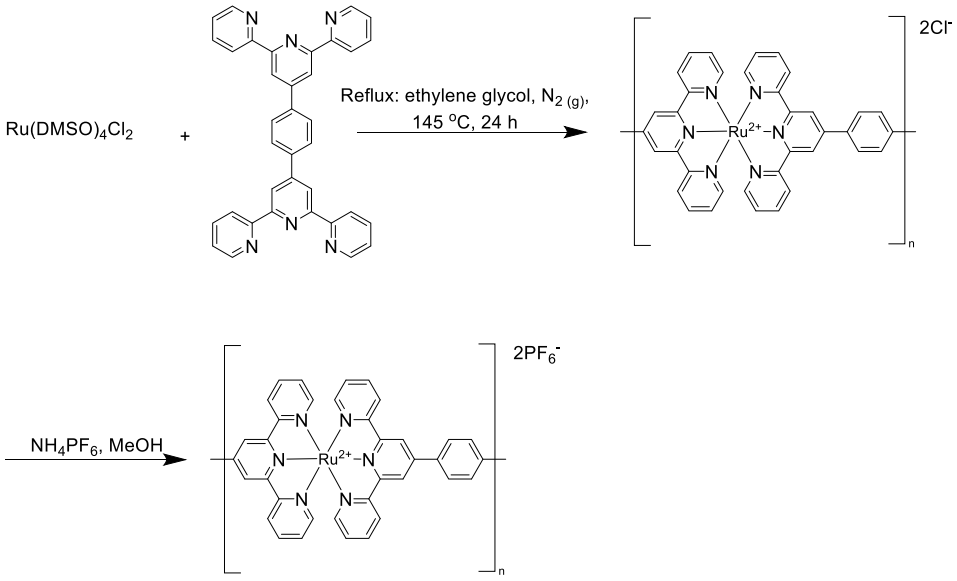

Figure 20. Synthesis and ion exchange of $[Ru^{II}\text{-tpy-ph-tpy}]_n(2Cl^-)_n$ to produce $[Ru^{II}\text{-tpy-ph-tpy}]_n(2PF_6^-)_n$.

3.1.1 Absorption Properties of $[Ru^{II}\text{-tpy-ph-tpy}]_n(2X)_n$

The UV-vis absorption spectra of $[Ru^{II}\text{-tpy-ph-tpy}]_n(2X^-)_n$ were collected in MeOH/H_2O (v/v =4:1) ($X=Cl^-$) and acetonitrile ($X=PF_6^-$) (figure 21). The coordination polymer with Cl^- counter ion exhibited intense absorption peaks at 308 and 507 nm corresponding to π-π* and MLCT transitions, respectively. Similar transitions at 307 and 508 nm were observed in the $X=PF_6^-$ absorption spectrum. The extinction coefficient (ε) of each peak was determined by the Beer-Lambert law, A = εlC, in which A is the absorbance, ε is the extinction coefficient, l is the path length (1 cm), and C is the concentration (10 μM). The HOMO-LUMO gap (E_g) was estimated via equation $E_g=(1240/\lambda)eV$.[41] The absorption and calculated values are listed in table_.

The use of different counterions has not been shown to directly influence the absorption properties of Ru^{II}-polypyridyl complexes.[42] However, these polymer complexes with PF_6^- counterions exhibit decreased solubility compared to those containing Cl^-.[43] Since the degree of polymerization is reversible and dependent on the concentration in solution,[44] the 1 nm red-shift of the MLCT from 507 to 508 nm, may be attributed to longer polymer lengths of the $[Ru^{II}\text{-tpy-ph-tpy}]_n(2PF_6^-)_n$. This would also explain the increase in MLCT ε from $4.39x10^4$ M^{-1} cm^{-1} ($X = Cl^-$) to $5.31x10^4$ M^{-1} cm^{-1} ($X = PF_6^-$) (table 2).

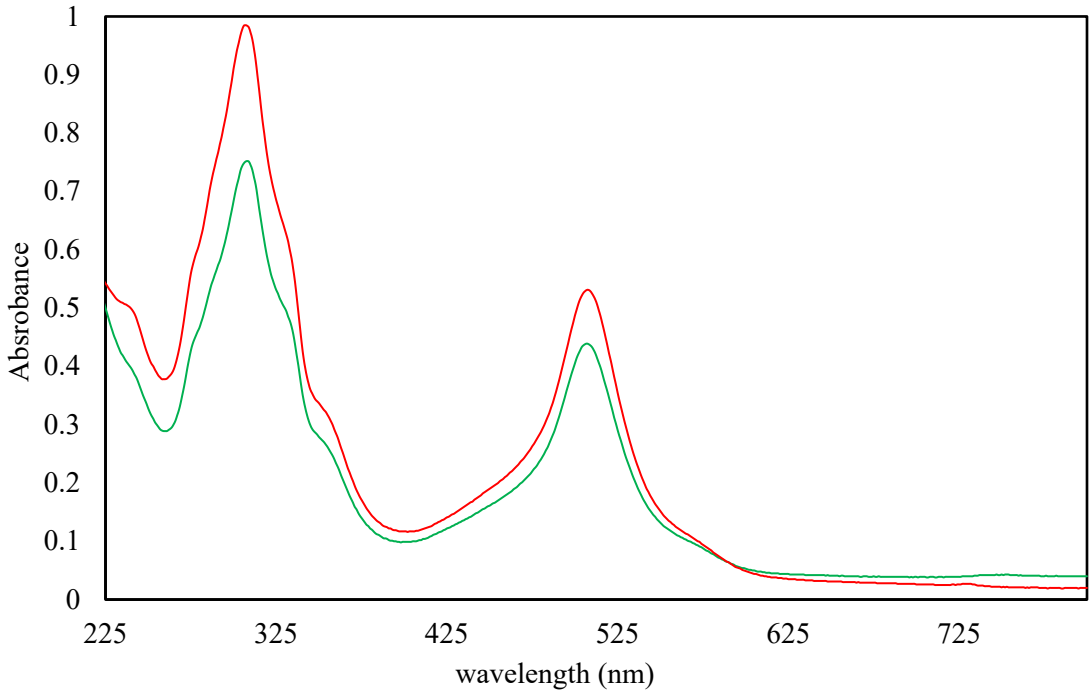

Figure 21. UV-vis absorption spectra of 10 µM $[Ru^{II}$-tpy-ph-tpy$]_n(2Cl^-)_n$ in $MeOH/H_2O$ (v/v=4:1) (green) and 10 µM $[Ru^{II}$-tpy-ph-tpy$]_n(2PF_6^-)_n$ in acetonitrile (red).

Table 2. Absorption data and estimated bandgaps of $[Ru^{II}$-tpy-ph-tpy$]_n(2X)_n$.

MOF (10 µM)	**π-π* λ_{max} (nm) (ε (M^{-1} cm^{-1}))**	**MLCT λ_{max} (nm) (ε (M^{-1} cm^{-1}))**	**E_g (eV) MLCT (π –π*)**
$[Ru^{II}$-tpy-ph-tpy$]_n(2Cl^-)_n$ $MeOH/H_2O$ (v/v =4:1) Green	308 (75200)	507 (43900)	2.446 (4.026)
$[Ru^{II}$-tpy-ph-tpy$]_n(2PF_6^-)_n$ Acetonitrile Red	307 (98500)	508 (53100)	2.441 (4.039)

3.1.2 Electrochemical Properties of $[Ru^{II}$-tpy-ph-tpy$]_n(2X)_n$

The energy levels of the HOMO (t_{2g}*) and LUMO (π*) molecular orbitals were determined via a cyclic voltammograms (CV) on a CHI411 electrochemical analyzer. The measurements were carried out using a three-probe system consisting of an

FTO/[Ru^{II}-tpy-ph-tpy]$_n$(2X)$_n$ working electrode, a platinum counter electrode, and a silver pseudo reference electrode. The working electrodes depicted in figure 22 were comprised of [Ru^{II}-tpy-ph-tpy]$_n$(2X)$_n$ drop cast onto the conductive side of blank FTO glass; concentrations were not important as multiple layers were applied until relatively even films developed. Polyimide tape was applied to the bottom of the FTO glass to prevent film deposition in these areas. Silver filled conductive epoxy was used to attach copper wire to the bare FTO glass, followed by 120 ºC curing in an oven (15 min). Capillary tubes and epoxy resin were used to seal away the copper wire and silver epoxy from the electrolyte solution. Electrolyte solutions of [Ru^{II}-tpy-ph-tpy]$_n$($2Cl^-$)$_n$ and [Ru^{II}-tpy-ph-tpy]$_n$($2PF_6^-$)$_n$ consisted of 0.1 M tetrabutylammonium hexafluorophosphate ($TBAPF_6$) dissolved in acetonitrile. A ferrocenium/ferrocene redox couple (Fc^+/Fc) (1 mM) was added to the electrolyte solution as an internal standard to calibrate the fluctuating potential of the pseudo reference electrode as Fc has a well-defined potential, 0.64 V vs SHE.[45,46] The CVs were performed in a potential window from 0 V to 2 V, starting from 0 in the positive direction at a scan rate of 50 mV/s.

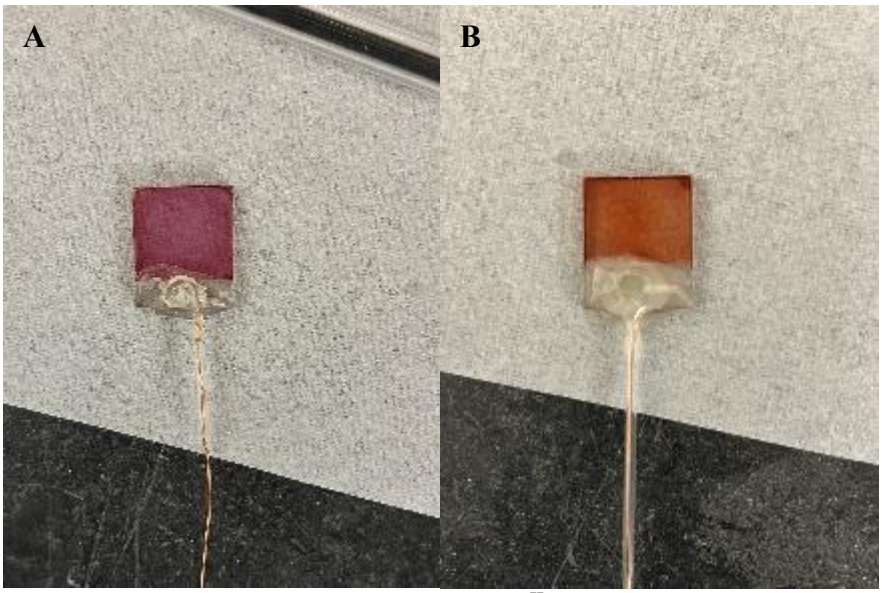

Figure 22. Working electrodes comprised of A) $[Ru^{II}\text{-tpy-ph-tpy}]_n(2Cl^-)_n$ and B) $[Ru^{II}\text{-tpy-ph-tpy}]_n(2PF_6^-)_n$ drop cast onto FTO glass.

The CVs of Fc and $[Ru^{II}\text{-tpy-ph-tpy}]_n(2X^-)_n$ are depicted in figure 23 and the potentials are tabulated in table 3. The oxidation (E_{ox}), reduction (E_{red}), and half-wave ($E_{1/2}$) potentials of Fc were 0.39 V, 0.27 V and 0.33 V, respectively. The $[Ru^{II}\text{-tpy-ph-tpy}]_n(2Cl^-)_n$ CV exhibited two E_{ox} peaks at 1.12 V and 1.34 V, and a single E_{red} peak at 1.11 V. In addition to prominent E_{ox} and E_{red} at 1.28 V and 1.08 V, the $[Ru^{II}\text{-tpy-ph-tpy}]_n(2PF_6^-)_n$ CV also demonstrated an additional E_{ox} at 1.04 V, albeit significantly less intense. In the CVs corresponding to $[Ru^{II}\text{-tpy-ph-tpy}]_n(2X^-)_n$, the E_{ox} peaks are attributed to the oxidation of the ruthenium's t_{2g}* molecular orbitals. Because the color of $[Ru^{II}\text{-tpy-ph-tpy}]_n(2X^-)_n$ films are due to the MLCT transitions,[47] oxidation of Ru^{II} to Ru^{III} were also visually indicated by a bleaching of the $[Ru^{II}\text{-tpy-ph-tpy}]_n(2X^-)_n$ films (figure 24). Notably, between the E_{ox} peaks of $[Ru^{II}\text{-tpy-ph-tpy}]_n(2Cl^-)_n$ and before the bleaching, a color change in the films from a purple red (figure 22A) to a brick red (similar to figure 22B) was observed that was attributed to ion exchange between the Cl^- in the film and the PF_6^- in the electrolyte solution; facile ion exchange by $[Ru^{II}\text{-tpy-ph-tpy}]_n(2X^-)_n$ has been

documented.[48] The final color of the film, as well as the second E_{ox} and the single E_{red} peaks that coincide with those in the $[Ru^{II}\text{-tpy-ph-tpy}]_n(2PF_6^-)_n$ CV, indicate that all but the initial E_{ox} peak in the $[Ru^{II}\text{-tpy-ph-tpy}]_n(2Cl^-)_n$ CV correspond to $[Ru^{II}\text{-tpy-ph-tpy}]_n(2PF_6^-)_n$. Moreover, shift from 1.12 V to 1.34 V upon ion exchange is indicative of a diffusion controlled redox process. CV scans with tetrabutylammonium chloride (TBACl) electrolyte were attempted to avoid ion exchange, however they were unsuccessful due to lack of solubility in acetonitrile. The initial E_{ox} peak in the $[Ru^{II}\text{-tpy-ph-tpy}]_n(2PF_6^-)_n$ CV is most likely due to minimal amounts of $[Ru^{II}\text{-tpy-ph-tpy}]_n(2Cl^-)_n$ trapped in the $[Ru^{II}\text{-tpy-ph-tpy}]_n(2PF_6^-)_n$ film.

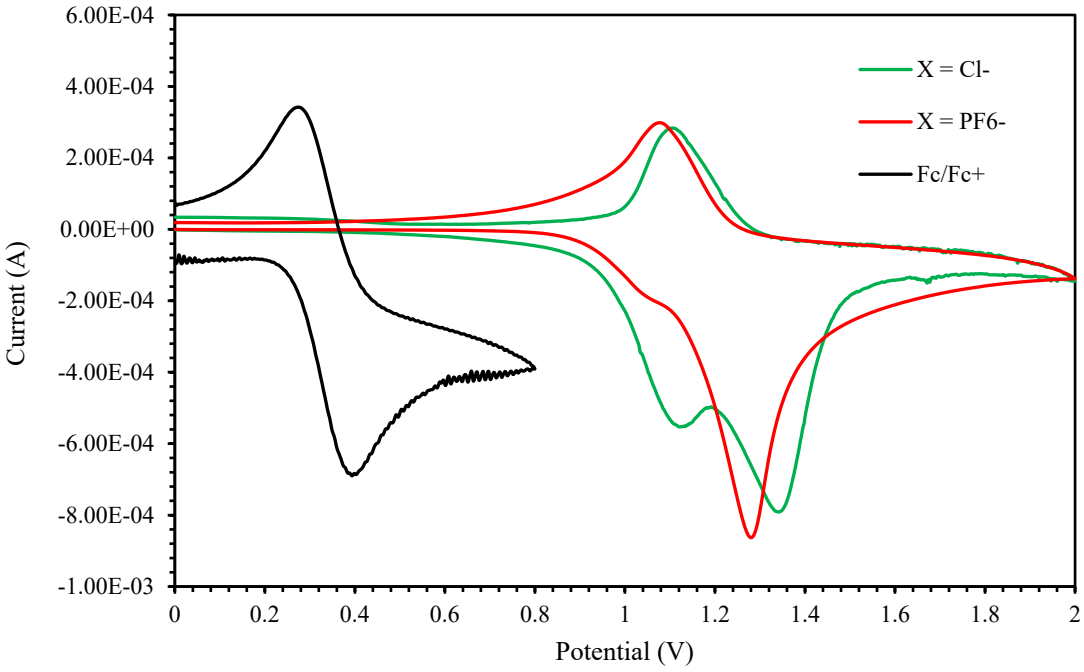

Figure 23. Cyclic voltammograms of Fc and $[Ru^{II}\text{-tpy-ph-tpy}]_n(2X^-)_n$ taken in 0.1 M $TBAPF_6$ in acetonitrile.

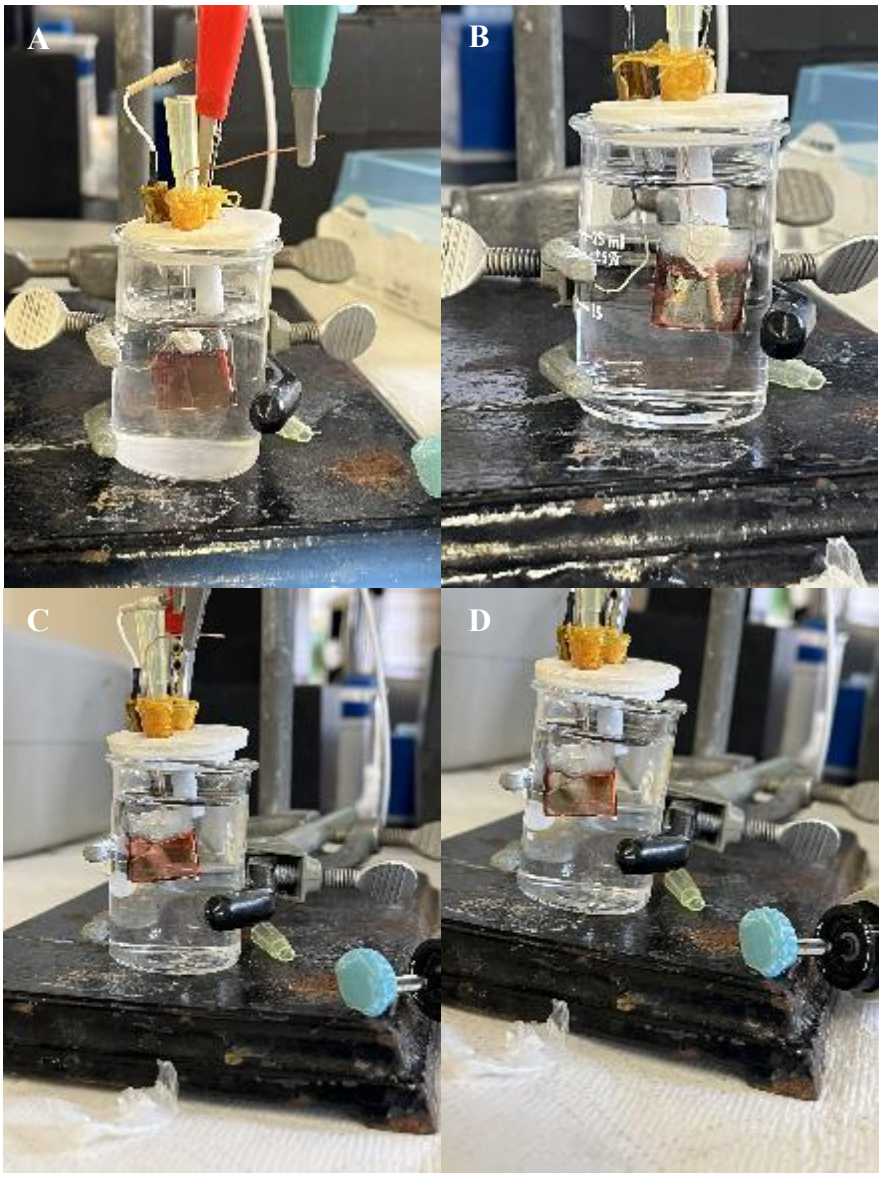

Figure 24. Experimental setup of the three-probe system. Working electrodes of A) FTO/[Ru^{II}-tpy-ph-tpy]$_n(2Cl^-)_n$ and C) FTO/[Ru^{II}-tpy-ph-tpy]$_n(2PF_6^-)_n$ before the start of the CV. Oxidation of the B) [Ru^{II}-tpy-ph-tpy]$_n(2Cl^-)_n$ and C) [Ru^{II}-tpy-ph-tpy]$_n(2PF_6^-)_n$ t_{2g}* molecular orbitals.

Table 3. Potentials (vs pseudo silver reference electrode) of $[Ru^{II}\text{-tpy-ph-tpy}]_n(2X)_n$

	E_{ox} (V)	E_{red} (V)	$E_{1/2}$ (V)
Ferrocene	0.39	0.27	0.33
X = Cl^-	1.12, 1.34	__, 1.11	__, 1.23
X = PF_6^-	1.04, 1.28	__, 1.08	__, 1.18

The HOMO and LUMO energy levels were determined utilizing the CVs and bandgaps determined via the UV-vis in chapter 3.1.1. The CVs were converted to the SHE scale, tabulated in table 4, by applying the Fc correction ($E_{1/2\ Fc\ vs\ SHE} = 0.64\ V - E_{1/2\ Fc\ vs\ Ag}$) to the measured CV values in table 3. The HOMO energy levels were determined by converting the HOMO potentials ($E_{1/2,\ ox\ vs\ SHE}$) to the absolute scale ($E_{HOMO} = -(E_{1/2,\ ox\ vs\ SHE} + 4.44)eV$) and the LUMO energy levels were determined by solving for E_{LUMO} in $E_g = E_{LUMO} - E_{HOMO}$. Example calculations for $[Ru^{II}\text{-tpy-ph-tpy}]_n(2Cl^-)_n$ are provided at the end of this section.

Table 4. Potentials (vs SHE) of $[Ru^{II}\text{-tpy-ph-tpy}]_n(2X)_n$ after Fc correction.

	E_{ox} (V)	E_{red} (V)	$E_{1/2}$ (V)
Ferrocene	0.70	0.58	0.64
X = Cl^-	1.43, 1.65	__, 1.42	__, 1.54
X = PF_6^-	1.35, 1.59	__, 1.39	__, 1.49

The band diagram in figure 25 compares the derived energy levels of $[Ru^{II}\text{-tpy-ph-tpy}]_n(2X^-)_n$ to those of anatase TiO_2, N719 dye, pure Spiro-MeOTAD, and Spiro-MeOTAD doped with LiTFSI and FK 209 Co(III) TFSI. The LUMO energy levels of

both $[Ru^{II}\text{-tpy-ph-tpy}]_n(2Cl^-)_n$ and $[Ru^{II}\text{-tpy-ph-tpy}]_n(2PF_6^-)_n$ were determined to be -3.53 eV and -3.49 eV, respectively; suitably aligned to facilitate electron injection into the TiO_2 CB (~ -3.94 eV)[15,49] and comparable to that of N719, E_{LUMO} ~ -3.01 eV.[50] The HOMO energy levels of $[Ru^{II}\text{-tpy-ph-tpy}]_n(2X^-)_n$, E_{HOMO} = -5.98 eV (X = Cl) and -5.93 eV ($X = PF_6^-$), also exhibited favorable alignment with the HOMO energy level of doped and undoped Spiro-MeOTAD, -5.4 eV and -5.0 eV, respectively.[51] This alignment is indicative of enabled facile regeneration of the $[Ru^{II}\text{-tpy-ph-tpy}]_n(2X^-)_n$ HOMO by the HTM. Furthermore, the HOMO energy levels of $[Ru^{II}\text{-tpy-ph-tpy}]_n(2X^-)_n$ may suggest an advantage of ssDSSCs sensitized with $[Ru^{II}\text{-tpy-ph-tpy}]_n(2X^-)_n$ over those sensitized with N719 as its HOMO level, -5.34 eV, is only favorably aligned with the undoped Spiro-MeOTAD. The lower HOMO energy levels of doped spiro-MeOTAD may allow for fabrication ssDSSCs with higher V_{oc}'s.

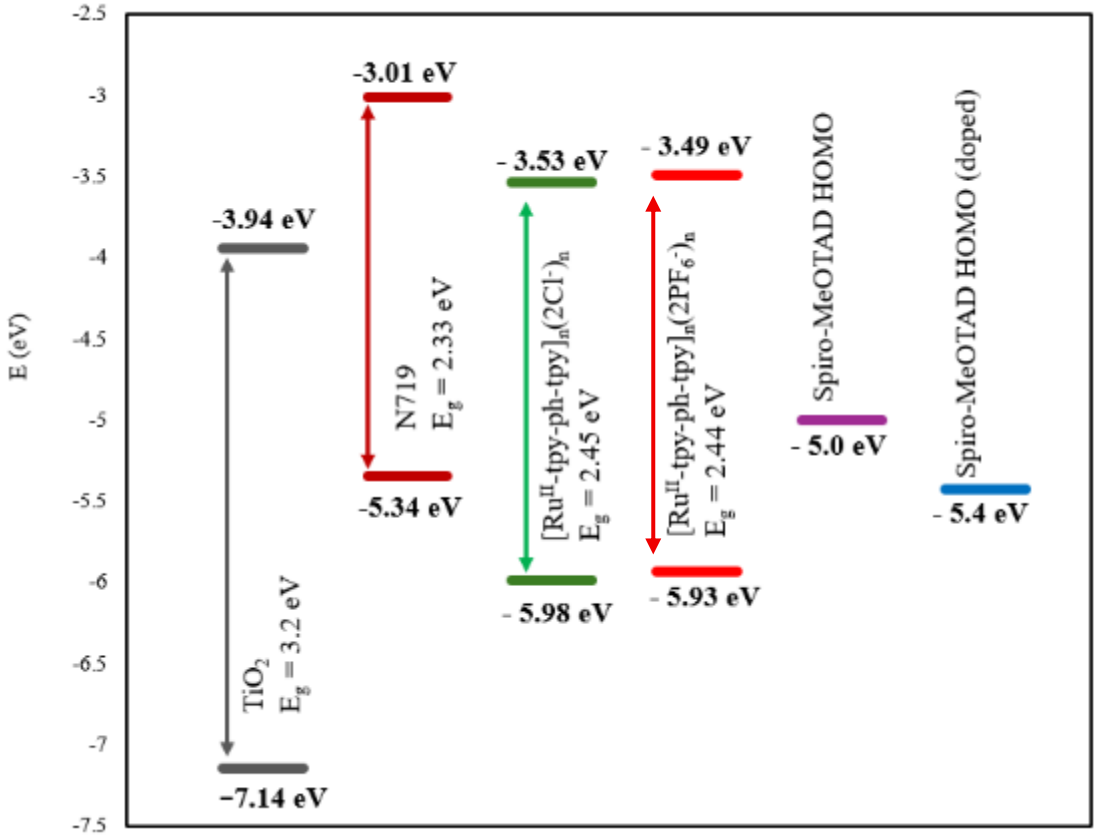

Figure 25. Energy band diagrams of anatase TiO_2, N719, $[Ru^{II}\text{-tpy-ph-tpy}]_n(2X^-)_n$, pure spiro-MeOTAD, and doped spiro-MeOTAD (LiTFSI, FK 209 Co(III) TFSI)

3.2 ssDSSC Fabrication

All ssDSSCs were fabricated on glass substrates coated with a conductive layer of fluorine-doped tin oxide (FTO). To control the area of the working electrode and to prevent short circuiting, etching was performed on the glass to remove the FTO layer outside of the working area. This was followed by solvent and plasma cleaning (optional), and the subsequent depositions of the following layers: TiO_2, anchor, $[Ru^{II}\text{-tpy-ph-tpy}]_n(2X)_n$ sensitizer, hole transporting material (HTM), and gold. A general description of the fabrication process is described below. More specific descriptions are provided in the results and discussion section.

3.2.1 Etching and Cleaning

A layer of polyimide tape was applied onto FTO glass substrates to protect the FTO beneath it from the etching process and the desired area of the working electrode was obtained by removing excess tape with a blade. The FTO glass was placed in a recrystallizing dish to which 2 M HCl was added until they were completely submerged. Enough zinc powder to coat the surface of each FTO glass was added immediately. The glass remained submerged for 1 minute after which the etching was stopped by neutralizing the HCl with sodium bicarbonate. Excess zinc was rinsed off with DI water, the glass was allowed to dry at room temperature, and a multimeter was used to determine the removal of the FTO layer by measuring the resistance. The polyimide tape was then removed to reveal a strip of FTO remaining down the center of the glass. The FTO glass will be referred to as cells, solar cells, or ssDSSCs from here on.

The cells were submerged in a beaker containing 1% micro soap and sonicated for 20 mins after which the micro soap solution was removed and the FTO glass was rinsed three times with DI water. These steps were repeated for each of the following: isopropanol, acetone, and DI water. Following the solvent cleaning, the cells were air dried and then subjected to plasma treatment via a PDC-32G plasma cleaner from Harrick Plasma. Initial plasma treatments used air as the plasma supply that was eventually replaced by $O_{2\,(g)}$ in the fabrication of the most recent cells. The etching and cleaning process are depicted in figure 26.

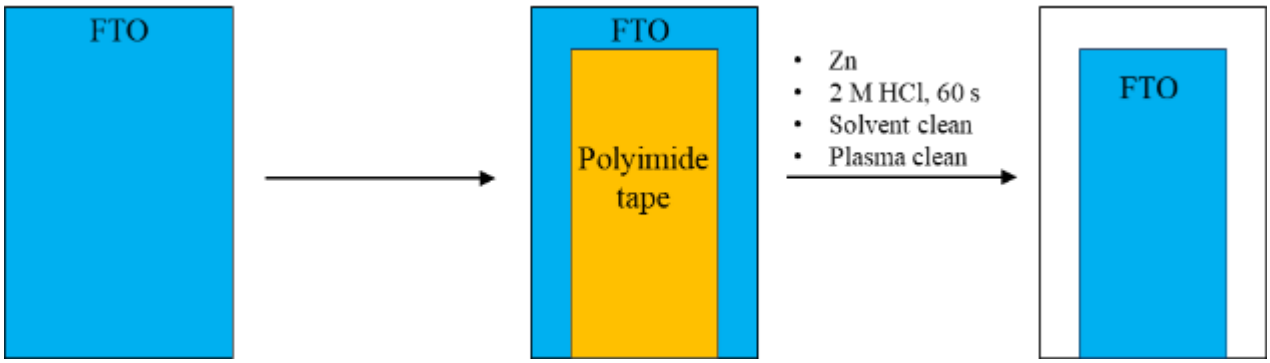

Figure 26. Diagram of the etching and cleaning process.

3.2.2 TiO_2 Semiconductor Synthesis and Deposition

A variety of ssDSSCs were fabricated consisting of compact TiO_2 layers synthesized directly onto the FTO glass through a sol-gel method ($TiO_{2\ comp}$) or a combination of TiO_2 particles ($TiO_{2\ part}$) that were synthesized separately and then deposited on top of the $TiO_{2\ comp}$. Before the deposition of TiO_2 layers, the bottom of the FTO glass was covered with polyimide tape to prevent layer formation in this area; it was left pristine to provide space for the connections during efficiency testing that will be discussed later (figure 27). After TiO_2 deposition, the polyimide tape was removed, and the cells were placed in a furnace with a set ramp rate of 5 ºC/min until a temperature of 500 ºC was reached. The cells were annealed at 500 ºC from 1 to 12 h. The temperature ranged widely because of the effects of time and temperature on TiO_2 crystallinity.

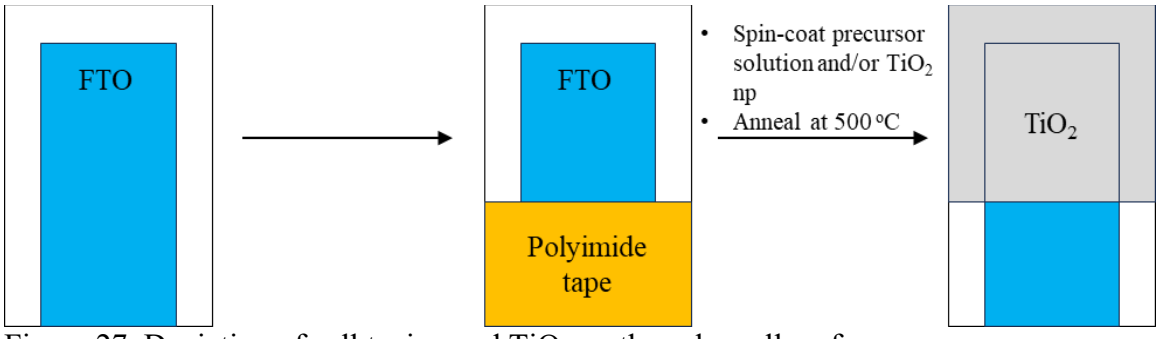

Figure 27. Depiction of cell taping and TiO_2 on the solar cell surface.

The precursor solution for $TiO_{2\ comp}$ was prepared in a glovebox under N_2. In a microwave vial, anhydrous isopropanol (6 mL), titanium n-butoxide (0.9 mL), and ethanolamine (0.19 mL) were mixed and sealed tightly. The mixture was removed from the glovebox, stirred and heated in an oil bath at 40 ºC for 2 h, cooled to room temperature, and stored at 4 ºC for 24 h before use. In a glovebox, the cells were placed on a spin-coater and a 1 mL syringe was used to deposit enough $TiO_{2\ comp}$ to cover the exposed glass. The cells were spin-coated at 2000 rpm for approximately 2 min and then removed from the glovebox and placed in the furnace for annealing. The entire deposition process was repeated for some sets of cells.

The $TiO_{2\ part}$ were prepared by adding a mixture of titanium n-butoxide (12.5 mL) and isopropanol (4 mL) dropwise to 0.1 M HNO_3 (150 mL) under vigorous stirring. The mixture formed a slurry that was heated in an oil bath at 80 ºC for 8 h. The slurry was hydrothermally autoclaved at 200 ºC for 12 h to produce the $TiO_{2\ part}$. Before deposition, the $TiO_{2\ part}$ were dispersed in solution via sonication with a Fisherbrand CPX2800 ULTRASONIC Bath for 1 h. The $TiO_{2\ part}$ were then deposited onto the cells with an airbrush and spin-coated at 2000 -3000 rpm.

3.2.3 Anchor molecule: 2,2':6',2''-terpyridine-4'-carboxylic acid

The $[Ru^{II}\text{-tpy-ph-tpy}]_n(2X)_n$ MOFs do not possess anchoring groups required to facilitate charge injection at the TiO_2/MOF interface and therefore adsorbing an anchor molecule onto the TiO_2 layer was necessary before MOF sensitization. The anchor molecule depicted in figure 28, 2,2':6',2''-terpyridine-4'-carboxylic acid ($^{-OOC}$tpy), was initially prepared in isopropanol however the solvent was changed to anhydrous EtOH to improve solubility. To enhance the formation of bidentate chelating bonds, the anchor

molecule was deprotonated by adding equimolar amounts of NaOH or KOH to the solution. To functionalize the TiO_2 surface with the anchor molecule cells were submerged anchor solution for 24-48 h (room temperature to 80 ºC), or, as the furnace cooled down from the annealing step, they were immediately submerged in anchor solution when they reached 80-100 ºC for 24-48 h.

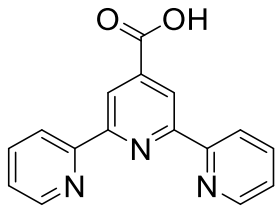

Figure 28. Anchor molecule, 2,2':6',2''-terpyridine-4'-carboxylic acid.

3.2.4 Molecular Wires Deposition

The synthesis of $[Ru^{II}\text{-tpy-ph-tpy}]_n(2X)_n$ is described in chapter 3.1. Solutions for the sensitization of ssDSSCs with $[Ru^{II}\text{-tpy-ph-tpy}]_n(2X)_n$ were prepared in MeOH ($X=Cl^-$) and acetonitrile ($X=PF_6^-$) with concentrations ranging from 0.3 mM to 4.6 mM. Deposition techniques include complete evaporation of solvents at different temperatures (room temp. to 80 ºC), incomplete evaporation of solvents (45-60 ºC), and heating cells in a pressure vessel (80 ºC). Polyimide tape was only applied to cells that were sensitized through room temperature evaporation. Aggregates were rinsed off the surface of the ssDSSCs with MeOH or acetonitrile.

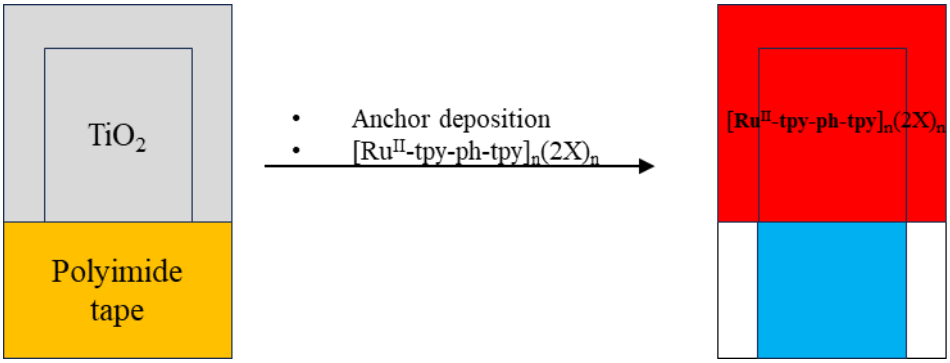

Figure 29. Deposition of $[Ru^{II}\text{-tpy-ph-tpy}]_n(2X)_n$.

3.2.5 HTM

In the glovebox, HTM was prepared by mixing 72.3 mg of Spiro-MeOTAD, 1 mL chlorobenzene, 10 mg of bis (trifluoromethane) sulfonimide lithium salt (LiTFSI), 10 mg of tris(2-(1*H*-pyrazol-1-yl)-4-*tert*-butylpyridine)cobalt(III) tri[bis(trifluoromethane)sulfonimide] (FK209 Co(III) TFSI), and 27 µL of tert-butyl pyridine in a microwave vial. The HTM was sonicated before use to fully dissolve the solid components. The HTM was spin-coated onto the ssDSSCs in the glovebox at 700-2000 rpm.

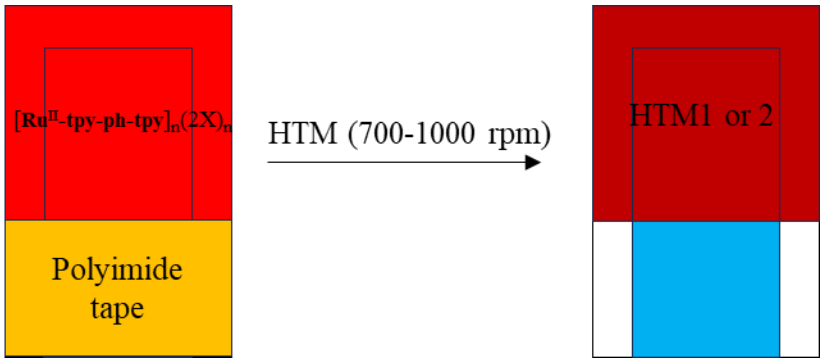

Figure 30. HTM deposition.

3.2.6 Gold

The ssDSSCs were completed by depositing a gold layer with a Cressington Sputter Coater 108 auto (100-150 s). Polyimide tape was used to keep the gold deposition

area centered on the part of the ssDSSC that contained all the following layers: FTO/TiO_2/$^{-OOC}$tpy/[Ru^{II}-tpy-ph-tpy]$_n$(2X)$_n$/HTM. Up until this point, the tape was placed at the border of the ssDSSC layers. This border was moved slightly further into the ssDSSCs layers to prevent contact between the gold and FTO (figure 31); contact between the two will short circuit the ssDSSC. A schematic of the ssDSSC cross section with speculated [Ru^{II}-tpy-ph-tpy]$_n$(2X)$_n$ orientation on the TiO_2 is depicted in figure 32.

Figure 31. Completion of ssDSSC after gold deposition.

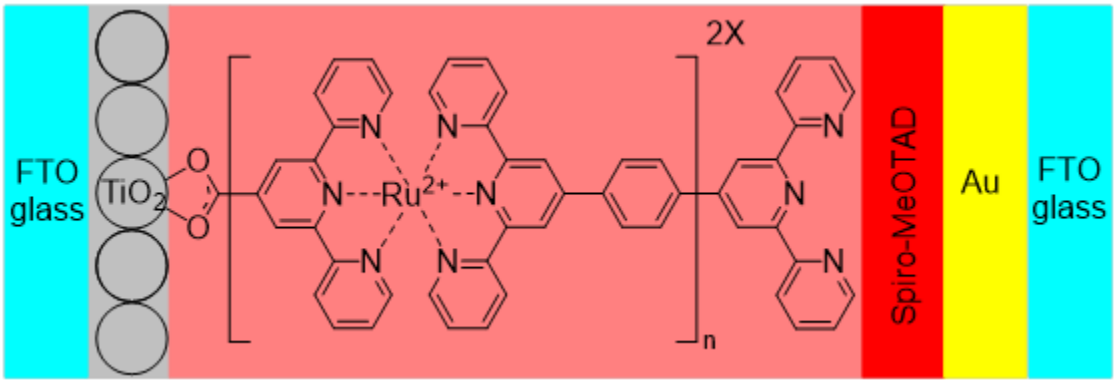

Figure 32. Schematic of a completed ssDSSC with [Ru^{II}-tpy-ph-tp]$_n$(2X)$_n$ (X is either Cl^- or PF_6^-) anchored to TiO_2 by $^{COO-}$tpy through a bidentate chelating bond

3.2.7 PCEs and OCVD measurements

PCEs were determined via a linear sweep voltammetry with a CHI832 electrochemical analyzer. This was accomplished by placing bare FTO glass on top of completed ssDSSCs to create direct contact between the gold and FTO layers. A mask was used to hold the completed ssDSSCs and bare FTO glass together and block the cells from incident light except for a 0.085 cm^2 window that exposed the backside of the ssDSSCs. The working electrode (black) was attached to the ssDSSCs and the reference (red) and counter electrodes (yellow) were attached to the bare FTO glass. While a lamp with a power source 0.137 W cm^2 illuminated the cells through the exposed window, a current-voltage (IV) curve was obtained as the current was measured against a sweeping voltage (0 -1.0V). JV curves were obtained by dividing every current value in the IV curve by the area of the window. FF and PCE were calculated with equations 1 and 2 from chapter 1.3.1.

The experimental setup to obtain the OCVD measurements was identical to that of the PCE experiment described above and depicted in figure_. Through an open circuit potential-time technique, the illumination on the ssDSSC was interrupted as described in chapter 1.3.2 and OCVD measurements were collected. Equations 3 and 4 were then applied to the OCVD measurements to determine the electron lifetime and recombination order β, respectively.

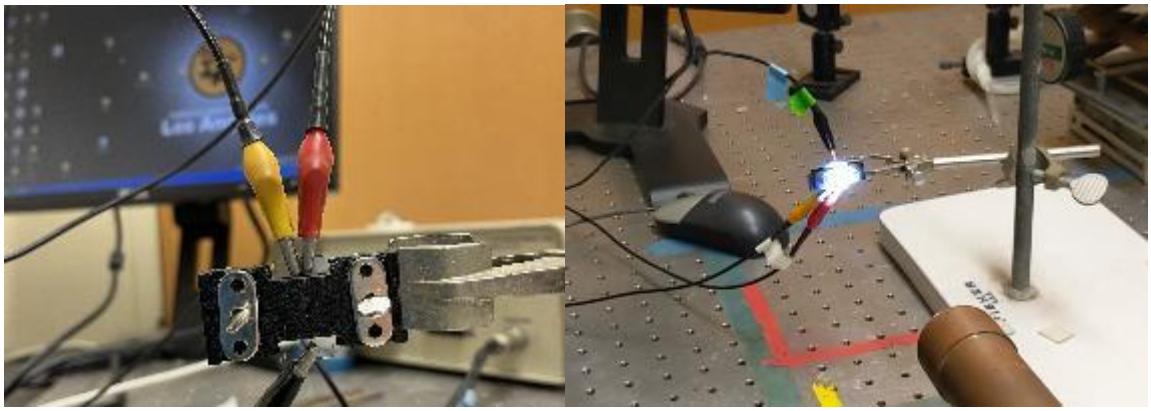

Figure 33. Linear sweep voltammetry and electron lifetime experimental setup on completed cells.

CHAPTER 4

RESULTS AND DISCUSSION

4.1 ssDSSC Performance

A variety of ssDSSCs were fabricated and tested. Only ssDSSCs with notable results that led to improvement of subsequent ssDSSCs will be discussed in this section. The performance parameters of all other cells are tabulated in table 6. The fabrication methods for all ssDSSCs are summarized in table 5.

4.1.1 Power Conversion Efficiency

The fabrication of ssDSSC A was the first to yield significant results (figure 34) with a V_{oc}, J_{sc} and PCE of -0.49 V, -3.14×10^{-6} A cm^{-2} and 2.48×10^{-4}%, respectively. The fabrication method included spin-coating the $TiO_{2\ comp}$ (2000 rpm) onto FTO glass and annealing at 500 ºC for 1 h. This was followed by submerging the cell in a 10 mM anchor solution (isopropanol) at room temperature overnight. The sensitizer layer was applied by submerging the cell in 1 mM $[Ru^{II}\text{-tpy-ph-tpy}]_n(2Cl^-)_n$ solution and completely evaporating the MeOH at 70 ºC. After, the HTM layer was spin-coated at 700-1000 rpm and allowed to dry overnight before the final gold layer was sputter-coated for 100 s. Despite its relatively high V_{oc} (by our standards), the ssDSSC's performance was overall suboptimal. A possible contributor to cell's low PCE was determined to be a lack of uniformity in the $[Ru^{II}\text{-tpy-ph-tpy}]_n(2Cl^-)_n$ layer (figure 35) which was due to the rapid evaporation of the MeOH during the deposition process. The purpose of applying heat to the $[Ru^{II}\text{-tpy-ph-tpy}]_n(2Cl^-)_n$ deposition step was to promote coordination with the anchor molecule. However, anchor adsorption onto the $TiO_{2\ comp}$ may have been limited due to its poor solubility in isopropanol.

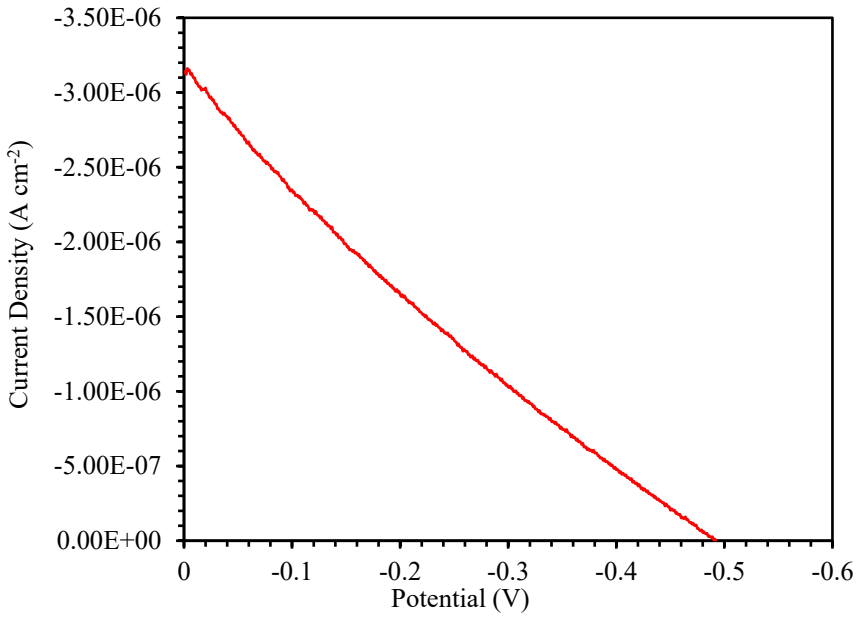

Figure 34. JV curve of ssDSSC A, the first solar to generate significant voltage and current.

Figure 35. Completed ssDSSC A.

The highest V_{oc} achieved was 0.71 V by ssDSSCs D2 and E; their JV curves are shown on figure 36. Solar cell D2 was fabricated by spin-coating (2000 rpm) and

annealing $TiO_{2\ comp}$ (500 ºC) for 1 h. The cell was then placed in a 1 mM anchor solution (anhydrous EtOH) and submerged at room temperature for 24 h. A 1 mM solution of $[Ru^{II}\text{-tpy-ph-tpy}]_n(2PF_6^-)_n$ was then drop cast at room temperature onto the surface of the $TiO_{2\ comp}$ layer. The HTM and gold layers were spin-coated at 700-1000 rpm and sputter-coated at 100 s, respectively. The fabrication of ssDSSC E was similar, except the cells were heated at 80 ºC while submerged in the anchor solution, and 1mM of $[Ru^{II}\text{-tpy-ph-tpy}]_n(2Cl^-)_n$ was drop cast onto the surface of the ssDSSC.

Despite their high V_{oc}'s, ssDSSC D2 exhibited a higher PCE ($2.14x10^{-3}$%) than ssDSSC E ($8.14x10^{-4}$%) due to the difference in J_{sc}; $-1.46x10^{-5}$ A cm^{-2} (D2) and $-7.36x10^{-6}$ A cm^{-2} I. This difference most likely stems from how the $[Ru^{II}\text{-tpy-ph-tpy}]_n(2X)_n$ layers aggregate on the $TiO_{2\ comp}$ surface. Figure 37 (left) shows that when $X = Cl^-$ the layers are relatively more uniform with some slightly denser areas. On the other hand, when $X = PF_6^-$, $Ru^{II}\text{-tpy-ph-tpy}]_n(2PF_6^-)_n$ forms densely packed ridges (figure 37 left) with lightly coated spaces in between.

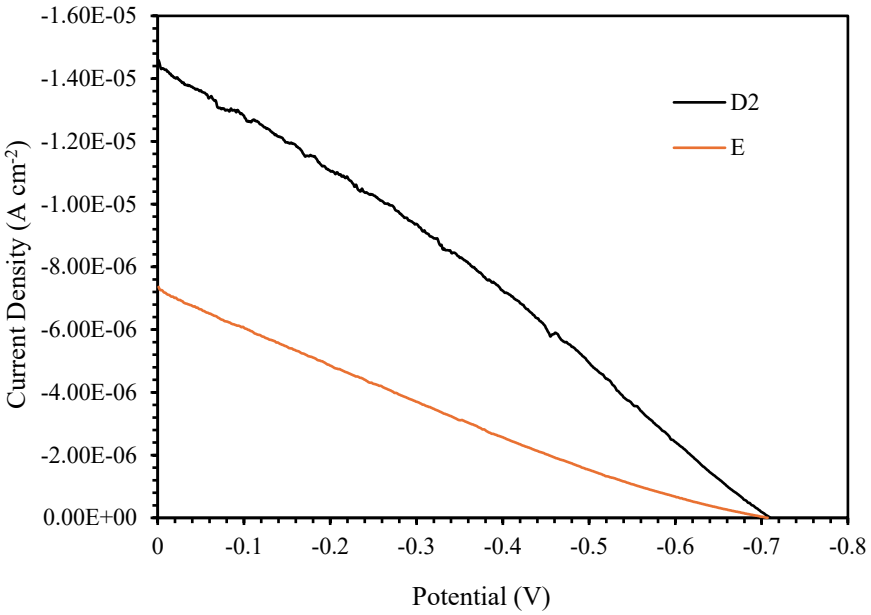

Figure 36. JV curves of ssDSSCs D2 and E; solar cells with the highest V_{oc} achieved (0.71 V).

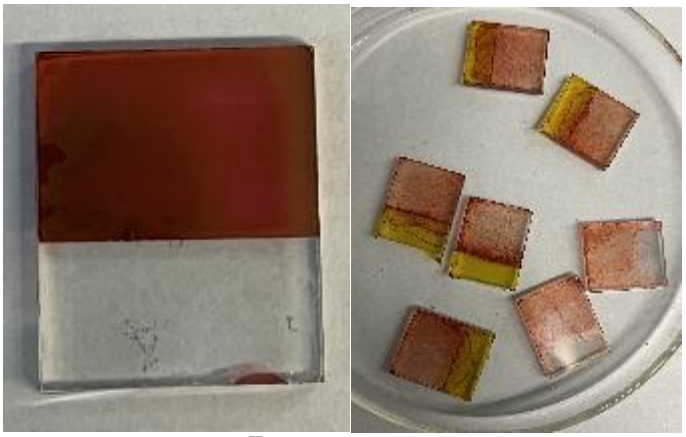

Figure 37. Uniform deposition of $[Ru^{II}\text{-tpy-ph-tpy}]_n(2Cl^-)_n$ (left) and visible aggregates of $[Ru^{II}\text{-tpy-ph-tpy}]_n(2PF_6^-)_n$ on $TiO_{2\ comp}$ (right).

It was speculated that either the anchor wasn't bonding to the $TiO_{2\ comp}$, wasn't coordinating to the $[Ru^{II}\text{-tpy-ph-tpy}]_n(2X)_n$, or both. To investigate this, ssDSSCs with and without anchor layers were fabricated. Two layers of $TiO_{2\ comp}$ were deposited onto FTO glass to increase the surface area and potentially anchor loading; each layer was spin-coated and annealed at 500 °C for 1 h. Anchor layers were deposited on ssDSSCs I and K by submerging them in a 2 mM anchor solution in anhydrous EtOH for 24 h at

room temperature. Solar cells J and L were not subjected to the anchor deposition process. 1 mM of $[Ru^{II}\text{-tpy-ph-tpy}]_n(2Cl^-)_n$ was drop cast onto ssDSSCs I and J, while 1 mM of $[Ru^{II}\text{-tpy-ph-tpy}]_n(2PF_6^-)_n$ was drop cast onto ssDSSC K and L. The HTM was spin-coated at 2000 rpm and the gold sputter-coating time was increased to 150 s to improve contact with the counter electrode.

There were no visible differences between ssDSSCs that did and did not contain an anchor layer (figure 38). The PCEs of ssDSSCs I, J, K and L were $3.46x10^{-3}$% (V_{oc} = -0.66 V, J_{sc} = $-3.04x10^{-5}$ A cm^{-2}), $4.86x10^{-3}$% (V_{oc} = -0.64 V, $-4.14x10^{-5}$ A cm^{-2}), $3.17x10^{-3}$% (V_{oc} = -0.48 V, J_{sc} = $-3.90x10^{-5}$ A cm^{-2}) and $3.64x10^{-3}$% (V_{oc} = -0.50 V, J_{sc} = $-4.59x10^{-5}$ A cm^{-2}), respectively. Even though the highest V_{oc}'s were achieved by ssDSSCs with $[Ru^{II}\text{-tpy-ph-tpy}]_n(2Cl^-)_n$, one of the overall highest V_{oc}'s achieved were sensitized with $[Ru^{II}\text{-tpy-ph-tpy}]_n(2PF_6^-)_n$, ssDSSC D2 with a V_{oc} of -0.71 V. Additionally, the ssDSSCs that did not undergo the anchor deposition step exhibited higher J_{sc}'s than their counterparts that did. Free anchor molecules dried on the $TiO_{2\ comp}$ surface may have prevented injection from $[Ru^{II}\text{-tpy-ph-tpy}]_n(2X)_n$ to the CB. Moreover, larger J_{sc}'s were also observed by ssDSSCs that utilized $[Ru^{II}\text{-tpy-ph-tpy}]_n(2PF_6^-)_n$, regardless of the anchor layer. These results suggest a lack of chemisorption between $[Ru^{II}\text{-tpy-ph-tpy}]_n(2X)_n$ and $TiO_{2\ comp}$. Generally, the purpose of the compact layer is to reduce recombination by blocking contact between the FTO glass and the redox mediator. For this reason, these layers are amorphous, densely packed and have a reduced surface area.

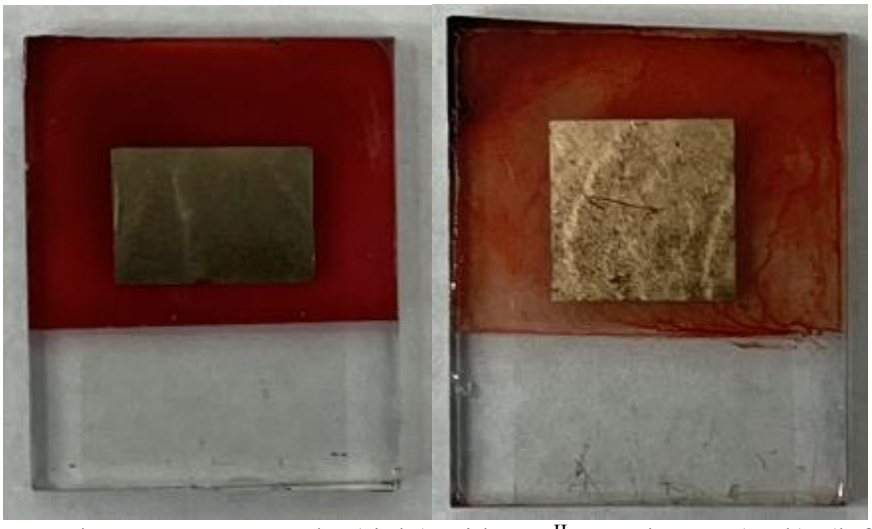

Figure 38. Complete ssDSSCs I and J (right) with $[Ru^{II}\text{-tpy-ph-tpy}]_n(2Cl^-)_n$ (left) and ssDSSCs K and L with $[Ru^{II}\text{-tpy-ph-tpy}]_n(2PF_6^-)_n$.

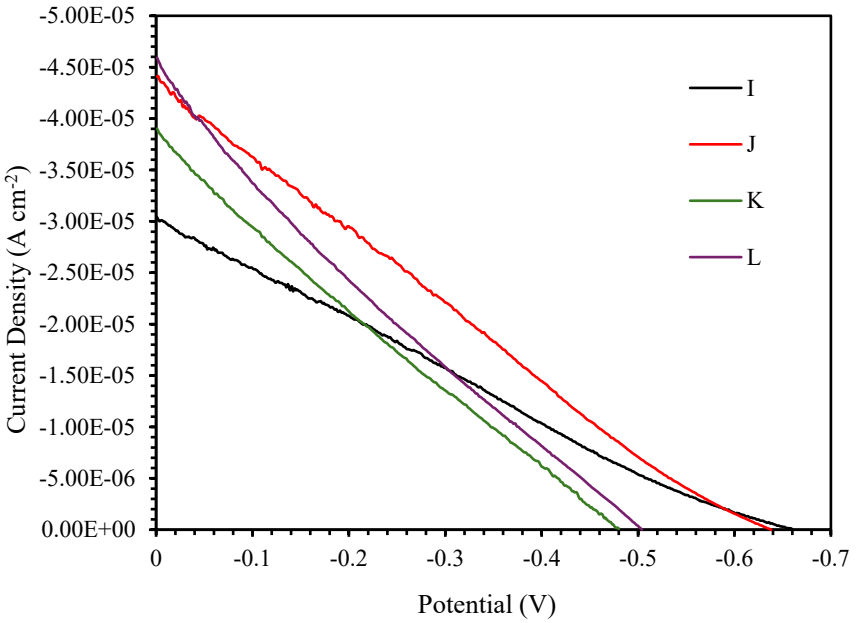

Figure 39. JV curves of ssDSSC I-L; a comparison of counterions (X = Cl^- or PF_6^-) and anchor on $TiO_{2\ comp}$.

The greatest impact on ssDSSC performance was due to the introduction of $TiO_{2\ part}$. For comparison, ssDSSC M1 was fabricated with two layers of $TiO_{2\ comp}$, while ssDSSCs M2 and M3 contained one layer of $TiO_{2\ comp}$ and one layer of $TiO_{2\ part}$. Each of the TiO_2 layers were spin-coated at 2000 rpm and annealed at 500 ºC for 12 h. Once the

ssDSSCs cooled down to 80-100 ºC, they were placed in a 1.5 mM anchor solution (in EtOH) containing equimolar amounts of KOH for 24 h. Solar cells M1 and M2 were placed in vials containing 0.3 mM $[Ru^{II}\text{-tpy-ph-tpy}]_n(2Cl^-)_n$, which were then placed in a beaker with MeOH that was covered with aluminum and heated at 45 ºC overnight (figure 40). This was done to slow down the evaporation of MeOH. Solar cell M3 was placed in a pressure vessel with 0.3 mM of $[Ru^{II}\text{-tpy-ph-tpy}]_n(2Cl^-)_n$ and heated at 90 ºC for 48 h. Solar cells M2 and M3 were rinsed with MeOH to remove any aggregates. This was attempted for solar cells in batch M1 but was not continued because these layers lacked stability and were easily rinsed off. For all ssDSSCs, the HTM was spin-coated at 2000 rpm and the gold was sputter-coated for 100 s.

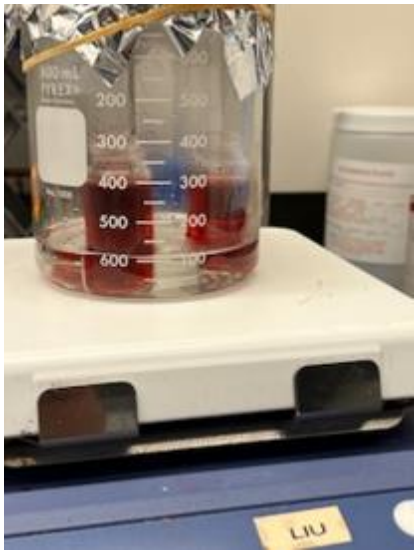

Figure 40. $[Ru^{II}\text{-tpy-ph-tpy}]_n(2Cl^-)_n$ deposition via solvent evaporation on ssDSSCs M1 and M2.

The performance parameters of ssDSSC M1 were consistent with the ssDSSCs that only contained $TiO_{2\ comp}$ and drop casted $[Ru^{II}\text{-tpy-ph-tpy}]_n(2X)_n$ layers; a PCE of $2.27x10^{-3}$%, a V_{oc} of -0.25 V and a J_{sc} of $-5.77x10^{-5}$ A cm^{-2}. On the other hand, regardless of deposition method, ssDSSCs M2 and M3 showed improvement. The PCE, V_{oc} and J_{sc}

parameters for ssDSSC M2 were $9.86x10^{-3}$%, -0.36 V and $-1.19x10^{-4}$ A cm^{-2}. For ssDSSC M3 they were $8.46x10^{-3}$%, -0.33 V and $-1.12x10^{-4}$ A cm^{-2}. Increases in J_{sc} were responsible for the improvements in PCE. The connection between J_{sc} and charge injection indicate adsorption between $TiO_{2\ part}$ and $[Ru^{II}\text{-tpy-ph-tpy}]_n(2Cl^-)_n$ through the anchor molecule. Additionally, ssDSSC M2 and M3 also demonstrated improved FF of 0.32 while the average thus far was 0.23.

To improve upon the fabrication methods, ssDSSC N2 was fabricated by increasing the anchor concentration and submergence time to 5 mM and 48 h. The concentration $[Ru^{II}\text{-tpy-ph-tpy}]_n(2Cl^-)_n$ was also increased to 4.6 mM and the layer was deposited by heating the cells at 90 ^oC for 48 h in a pressure vessel. This further increased the PCE, V_{oc}, and FF to $1.07x10^{-2}$%, -0.48 V, and 0.33. The J_{sc} decreased to $-9.30x10^{-5}$ A cm^{-2}. Solar cell N1 was fabricated to test drop casting $[Ru^{II}\text{-tpy-ph-tpy}]_n(2X)_n$ on $TiO_{2\ part}$. The PCE, V_{oc} and J_{sc} were $2.46x10^{-4}$%, -0.34 V and $-4.51x10^{-6}$ A cm^{-2}. Out of all the reported cells in table 6, this one was the worst. Its parameters were similar to ssDSSC A. The inclusion of a $TiO_{2\ comp}$, $TiO_{2\ part}$, and $[Ru^{II}\text{-tpy-ph-tpy}]_n(2Cl^-)_n$ layers may have hindered charge mobility, or the solar cell was defective.

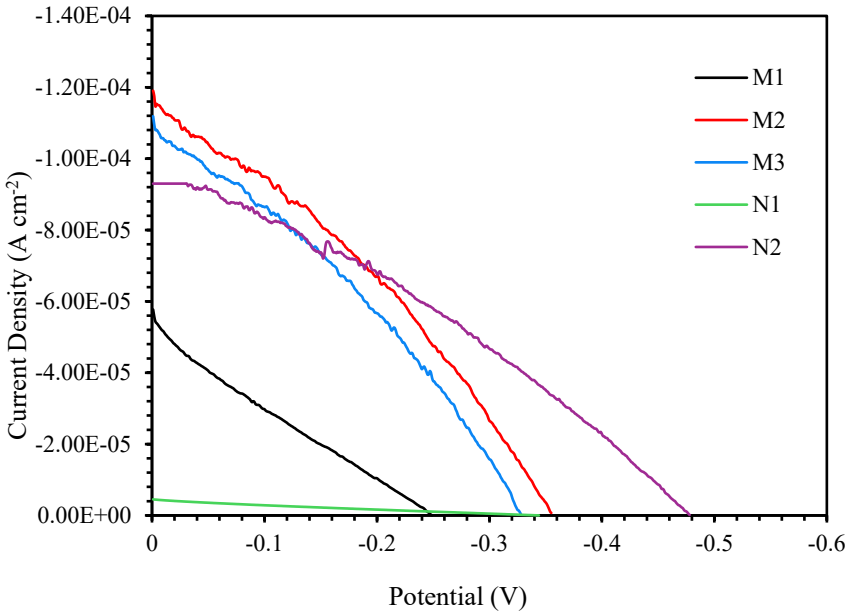

Figure 41. JV curves of ssDSSCs M and N.

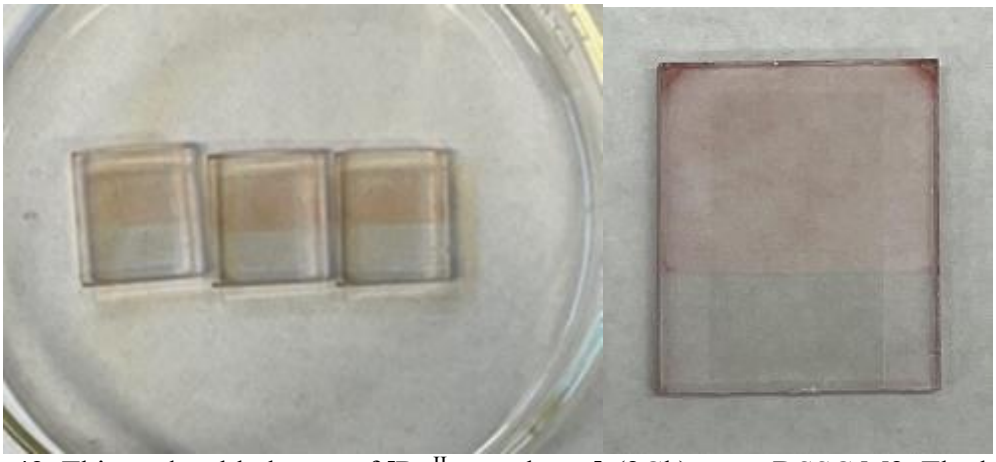

Figure 42. Thin and stable layers of $[Ru^{II}\text{-tpy-ph-tpy}]_n(2Cl^-)_n$ on ssDSSC M2. The layer thickness of ssDSSC M3 was identical (left). Slightly darker $[Ru^{II}\text{-tpy-ph-tpy}]_n(2Cl^-)_n$ layer on ssDSSC N2 (right).

The syntheses of Ru^{II}-terpyridine complexes are typically carried out under elevated temperatures and under inert conditions with dry solvents. Previous attempts to grow $[Ru^{II}\text{-tpy-ph-tpy}]_n(2Cl^-)_n$ on the $TiO_{2\ comp}$ include placing $FTO/TiO_{2\ comp}/^{(H)OOC}$tpy inside a round bottom flask and performing the synthesis described in chapter 3.1, or by placing $FTO/TiO_{2\ comp}/^{(H)OOC}$tpy in previously synthesized $[Ru^{II}\text{-tpy-ph-tpy}]_n(2Cl^-)_n$

dissolved in anhydrous ethylene glycol and refluxing for 24 h at 145 ºC under N_2. These methods were unsuccessful and therefore were not included in tables 5 or 6. This was most likely attributed to the $TiO_{2\ comp}$ and it may be worth revisiting using solar cells with $TiO_{2\ part}$ layers. Solar cells O and P consisted of $TiO_{2\ comp}$ and $TiO_{2\ part}$ annealed for 12 h and 1 h, respectively. The anchor deposition process was similar to that of ssDSSC N2 except these cells were held in the solution for 48 h. Solar cells O ($X = Cl^-$) and P ($X = PF_6^-$) were sensitized by refluxing them in $[Ru^{II}\text{-tpy-ph-tpy}]_n(2X)_n$ dissolved in dry MeOH (70 ºC) or acetonitrile (90 ºC) under N_2 for 48 h. The HTM was spin-coated at 2000 rpm and the gold was sputter-coated for 100 s.

Figure 43 depicts the JV curves of ssDSSCs O and P. Compared to the previous ssDSSCs, solar cell O demonstrated a relatively high PCE of $9.73x10^{-3}$% that was in line with solar cells fabricated with similar $[Ru^{II}\text{-tpy-ph-tpy}]_n(2X)_n$ deposition techniques, ssDSSCs M2, M3 and N2. Its V_{oc} (-0.34 V), J_{sc} ($-1.07x10^{-4}$ A cm^{-2}) and FF (0.36) were also consistent with the previously high performing solar cells. Solar cell P had a PCE of $1.62x10^{-2}$%, the highest achieved so far. Its high PCE was due to increases in its FF (0.42) and J_{sc} ($-1.42x10^{-4}$ A cm^{-2}) which were also the highest so far.

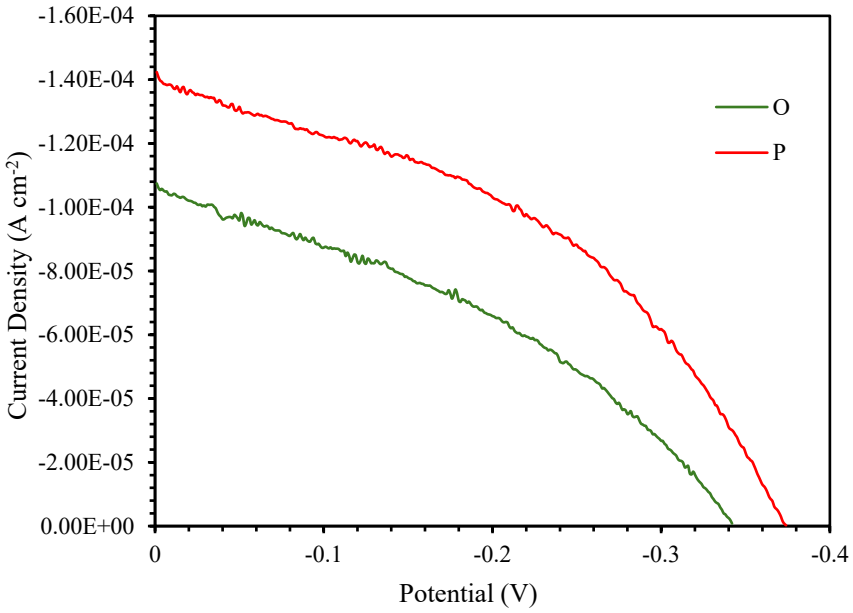

Figure 43. JV curves of ssDSSCs O and P.

Ideally, the ssDSSC JV curves should resemble that of a diode in which current flows in one direction and is blocked in the opposite direction, the gray curve in figure 44. Such behavior is indicative of low series resistance (R_S) and high shunt resistance (R_{SH}).[52] This is because large R_S is indicative of high resistivity in the absorber material (vertical) or poor contact between the interfacing layers (lateral). On the other hand, a large R_{SH} is indicative of the absence of charge leaking pathways such as pinholes or recombination sites. In a JV curve, a large R_S is represented as a less steep slope at the V_{oc}, and a low R_{SH} is observed as a less flat curve at the J_{sc}. This results in an s-shaped JV curve with a lower FF and PCE, the red curve in figure 44. All the solar cells fabricated in this work, including ssDSSCs M2, M3, N2, O and P but to a lesser extent, had s-shaped JV curves. In ssDSSCs whose $[Ru^{II}\text{-tpy-ph-tpy}]_n(2X)_n$ layers were drop cast on, it is likely that R_S, as a result of thicker layers, is in part responsible for the s-shape curves. Additionally, recombination as a result of these thick layers, as well as the inevitable

formation of pinholes during the fabrication process, also contributed to the s-shape by decreasing R_{SH}.

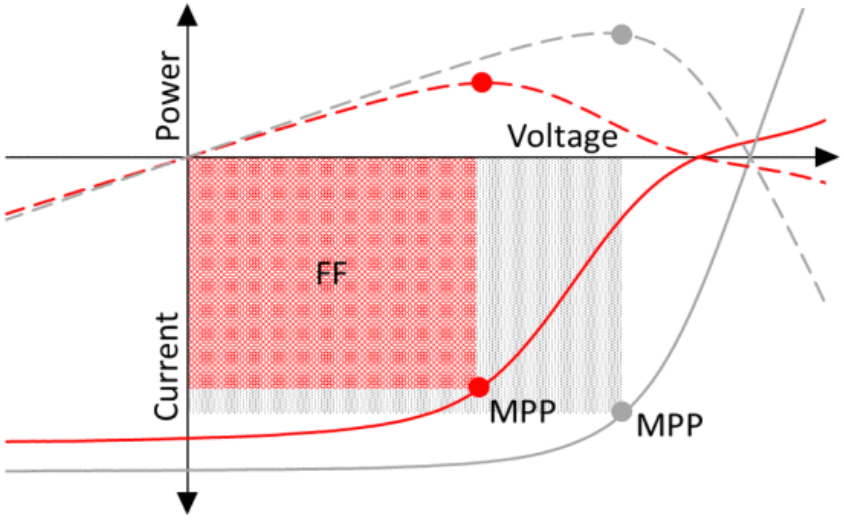

Figure 44. An ideal IV curve (gray) and an s-shaped IV curve (red).[52]

4.1.2 OCVD, Lifetime and Recombination Order Measurements

The OCVD curve of ssDSSC E, depicted in figure 45, shows an initial slow decay that increases slightly until the end of the 30 s measurement. The overall shallow OCVD curve and the relatively high final V_{oc} (~0.7 V) indicate long τ_n in E and was confirmed in the τ_n measurements in figure 46; the steep plot shows small changes in V_{oc} relative to larger increases in τ_n. Additionally, the non-linear logarithmic dependence of τ_n on V_{oc} suggests multiple recombination processes occurring within the solar cell.[53] Figure 47 confirms these processes to be trap-mediated/Shockley-Read-Hall ($\beta = 1$), band-to-band/bimolecular ($\beta = 2$), Auger ($\beta = 3$) and more complex recombination mechanisms ($\beta > 3$).[54] The introduction of trap states in TiO_2 is due to imperfections in the manufacturing process and therefore Shockley-Read-Hall recombination was unavoidable in all ssDSSCs. Likewise, because of interfacial contact between TiO_2 and $[Ru^{II}$-tpy-ph-tpy$]_n(2X)_n$, and/or TiO_2 and the HTM, direct bimolecular recombination was also present

in E and all ssDSSCs fabricated. Auger recombination, however, only occurs in the presence of high charge concentrations. In ssDSSC E, high electron concentrations in the $TiO_{2\ comp}$ were indicated by the high V_{oc} at the end of the OCVD measurement. This was likely due to trapped electrons due to the large R_S in the thick $[Ru^{II}\text{-tpy-ph-tpy}]_n(2Cl^-)_n$ layer.

The OCVD measurement of ssDSSC D2 in figure 45 also indicates a slower initial decay, however, the decay increase is greater and more consistent. This is observed in the slightly longer τ_n from ~ -0.75 V to ~ -0.72 V in figure 46, followed by a linear logarithmic dependance of τ_n on V_{oc}. Figure 47 shows that in ssDSSC D2, a slower trap-mediated recombination process dominates at larger V_{oc} ($\beta < 1$) and transitions to more consistent process with trap-mediated and bimolecular contributions ($\beta \sim 1.6$). Although the relatively large final V_{oc} in the OCVD measurements still reflect a delayed recombination process due to high R_S in the $[Ru^{II}\text{-tpy-ph-tpy}]_n(2PF_6^-)_n$ layer, it is likely that the less uniform $[Ru^{II}\text{-tpy-ph-tpy}]_n(2PF_6^-)_n$ layer allowed for greater contact between the $TiO_{2\ comp}$ and HTM and therefore bimolecular recombination was a dominant mechanism.

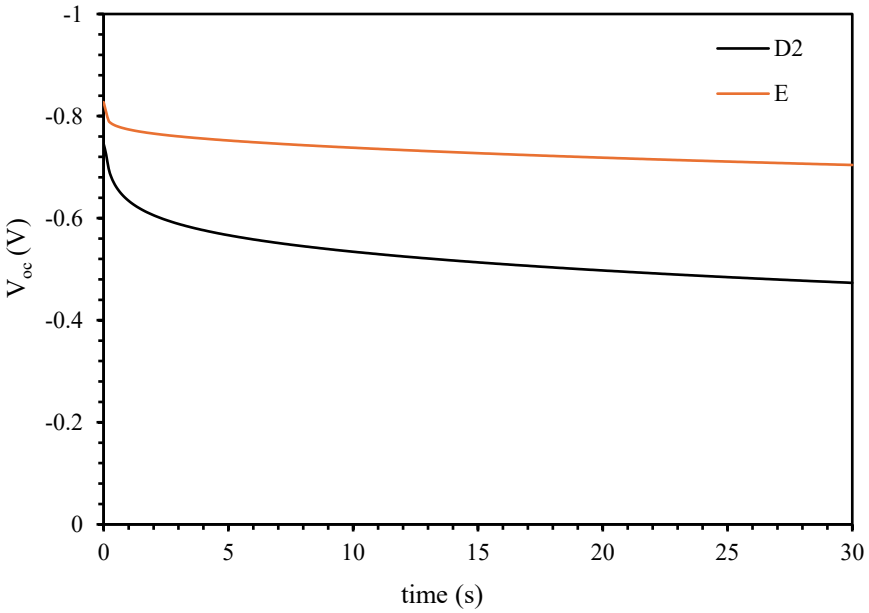

Figure 45. OCVD measurements of ssDSSCs D2 and E.

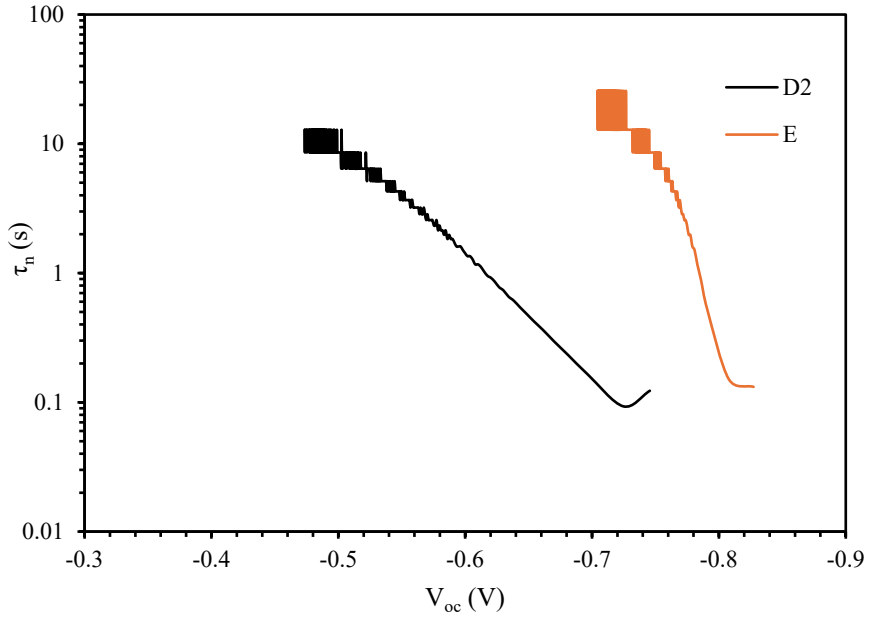

Figure 46. Lifetime measurements of ssDSSC D2 and E.

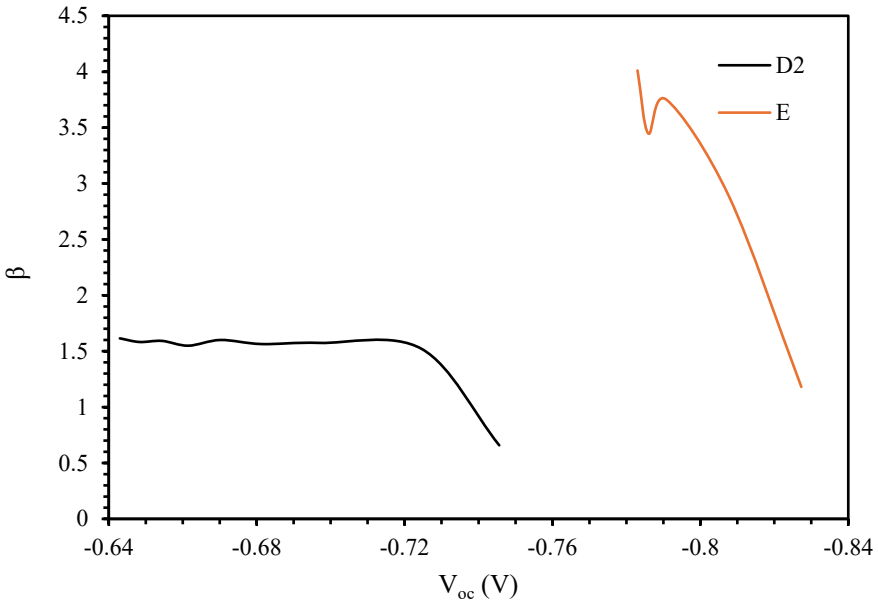

Figure 47. Recombination order of ssDSSCs D2 and E.

The initial high V_{oc} in the OCVD measurements, slow decay and relatively long τ_n of ssDSSCs E and D2 were mainly due to deposition methods that resulted in thick $[Ru^{II}\text{-tpy-ph-tpy}]_n(2X)_n$ layers. This behavior was also observed in ssDSSCs I-L in which all $[Ru^{II}\text{-tpy-ph-tpy}]_n(2X)_n$ layers were dropped cast onto $TiO_{2\ comp}$. The OCVD measurements in figure 48 show consistency between I and J but not K and L. This may be due to greater uniformity of the $[Ru^{II}\text{-tpy-ph-tpy}]_n(2X)_n$ layer when $X = Cl^-$ than when $X = PF_6^-$; the large initial V_{oc} in ssDSSCs I and J was likely due to increased $TiO_{2\ comp}$ and $[Ru^{II}\text{-tpy-ph-tpy}]_n(2Cl^-)_n$ contact, regardless of whether or not they underwent the anchor deposition step. The overall rates of decay were I>J>K>L and are demonstrated in figure 49 as longer τ_n for ssDSSCs with slower decaying OCVD measurements. Figures 49 and 50 also indicate multiple recombination processes in sDSSCs I ($\beta \sim 1.1\text{-}1.8$), J ($\beta \sim 0.6\text{-}2.1$) and L ($\beta \sim 1.5\text{-}2.8$). Solar cells I and J exhibited the expected trap-mediated and bimolecular processes; their fast relatively faster recombination kinetics are due to the large concentration of charges in the $TiO_{2\ comp}$ CB. Although the lower V_{oc} of ssDSSC

L reflects lower initial charge concentrations when compared to I and J, the brief Auger recombination contribution may be explained by the slow recombination kinetics in L. Figure 50 indicates the dominant recombination process in ssDSSC K to be mainly bimolecular ($\beta \sim 1.8$-2.0) at higher V_{oc}. A large noise to signal ratio is typically expected at lower V_{oc} in τ_n measurements as recombination slows down however, the excessive noise in ssDSSC K was likely due to experimental error.

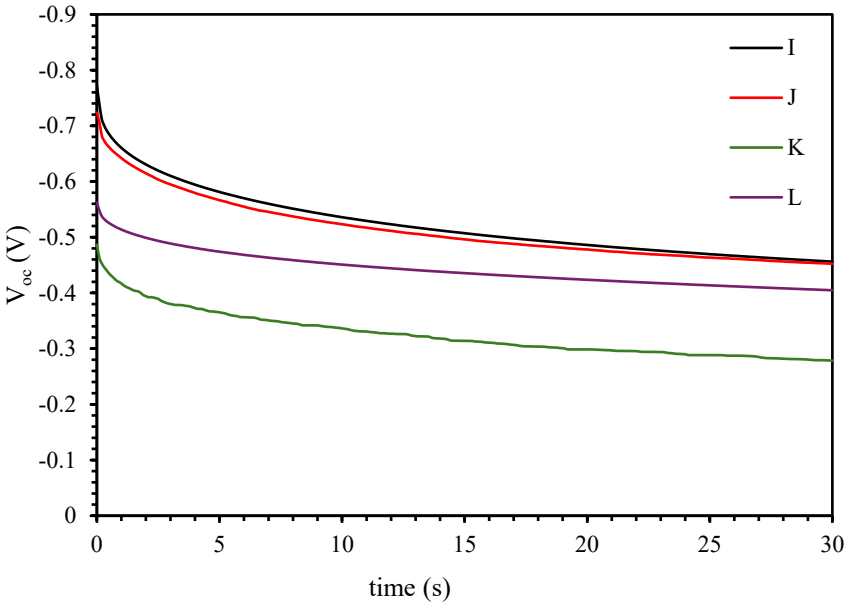

Figure 48. OCVD measurements of ssDSSCs I-L.

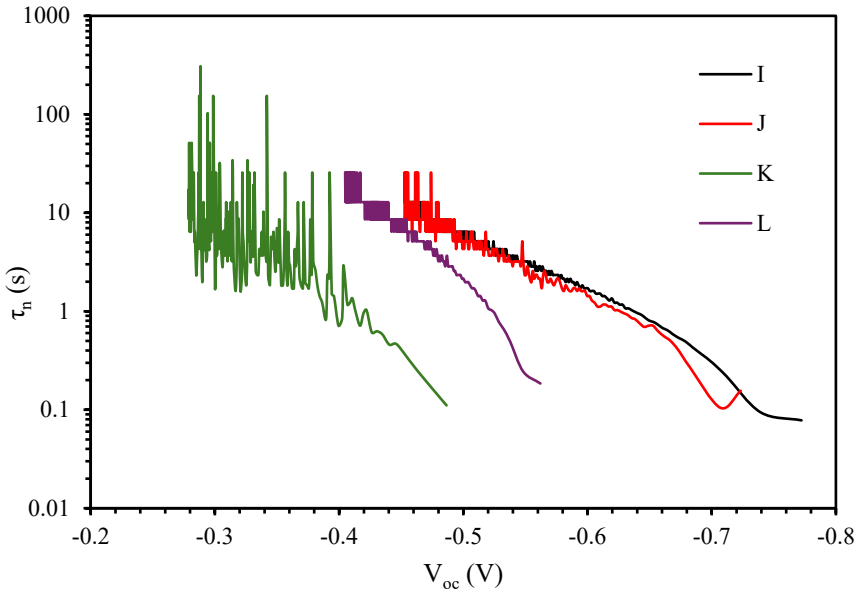

Figure 49. Lifetime measurements of ssDSSC I-L.

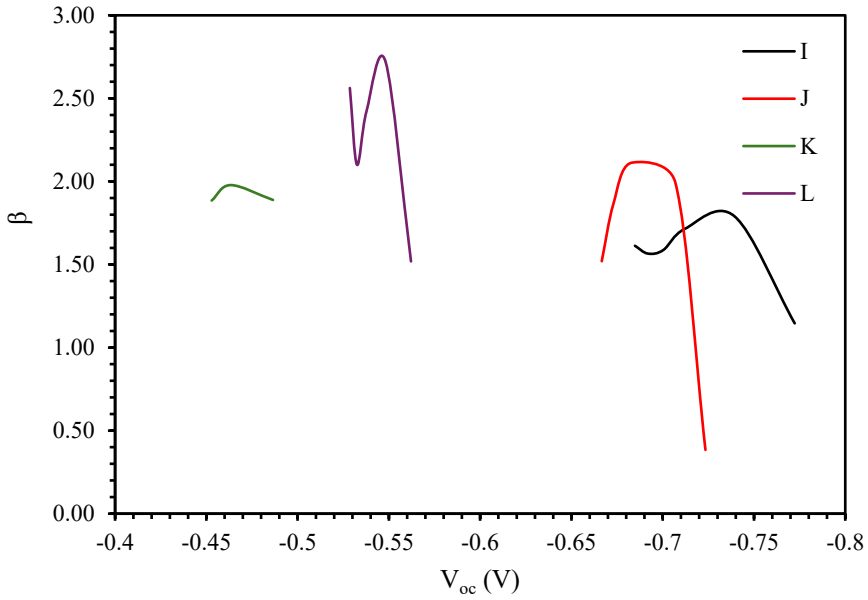

Figure 50. Recombination order of ssDSSCs I-L.

Solar cell M1 had the slowest recombination kinetics. Poor electron injection as a result of insufficient adsorption of $[Ru^{II}\text{-tpy-ph-tpy}]_n(2Cl^-)_n$ onto the $TiO_{2\ comp}$ layers was a major contributor as recombination rates depend on electron density in the TiO_2 CB.

This is evident by the low J_{sc} in figure 41 and low the low initial V_{oc} in the OCVD measurements (figure 51). The initial longer τ_n at higher V_{oc}'s suggests trap-mediated recombination. The transition to a steeper, logarithmically linear τ_n plot (figure 52), as well as the recombination order measurements in figure 53, indicate a transition to a dominant bimolecular recombination mechanism ($\beta \sim 2$), with $[Ru^{II}\text{-tpy-ph-tpy}]_n(2Cl^-)_n$ or HTM directly, as V_{oc} decreases. Figure 53 shows that recombination with the HTM or $[Ru^{II}\text{-tpy-ph-tpy}]_n(2Cl^-)_n$ was also a dominant process in ssDSSCs M2 and M3. In all three cases, thinner $[Ru^{II}\text{-tpy-ph-tpy}]_n(2Cl^-)_n$ layers allow for increased TiO_2/$[Ru^{II}\text{-tpy-ph-tpy}]_n(2Cl^-)_n$/HTM contact. The larger initial V_{oc}'s of M2 and M3 in figure 51 when compared to M1 can be attributed to increased charge injection as a result of enhanced $TiO_{2\ part}$/$[Ru^{II}\text{-tpy-ph-tpy}]_n(2Cl^-)_n$ adsorption. The increased electrons in the TiO_2 CB of M2 and M3 are responsible for the increased recombination kinetics in the OCVD and τ_n curves. The large initial V_{oc} of ssDSSC N1 was attributed to the increased TiO_2 surface area coverage by $[Ru^{II}\text{-tpy-ph-tpy}]_n(2Cl^-)_n$ due to the drop casting deposition. Similar to the previous solar cells that utilized this deposition method, high charge concentration allowed for some Auger recombination contribution (figure 53). Solar cell N2 had significantly less $[Ru^{II}\text{-tpy-ph-tpy}]_n(2Cl^-)_n$ in contact with the $TiO_{2\ part}$ surface, yet its initial V_{oc} was comparable to that of N1 (figure 51). This was a result of increased charge injection due to the inclusion of the $TiO_{2\ part}$ and improved $[Ru^{II}\text{-tpy-ph-tpy}]_n(2Cl^-)_n$ deposition. The rapid decay in the OCVD curve is attributed to increased electron density in the TiO_2 CB and increased contact at TiO_2/$[Ru^{II}\text{-tpy-ph-tpy}]_n(2Cl^-)_n$/HTM interface. The consistent τ_n and β (~1.5) in figures 52 and 53, respectively, show a mixture of trap-mediated ($\beta = 1$) and bimolecular ($\beta = 2$) recombination processes in ssDSSC N2.[54]

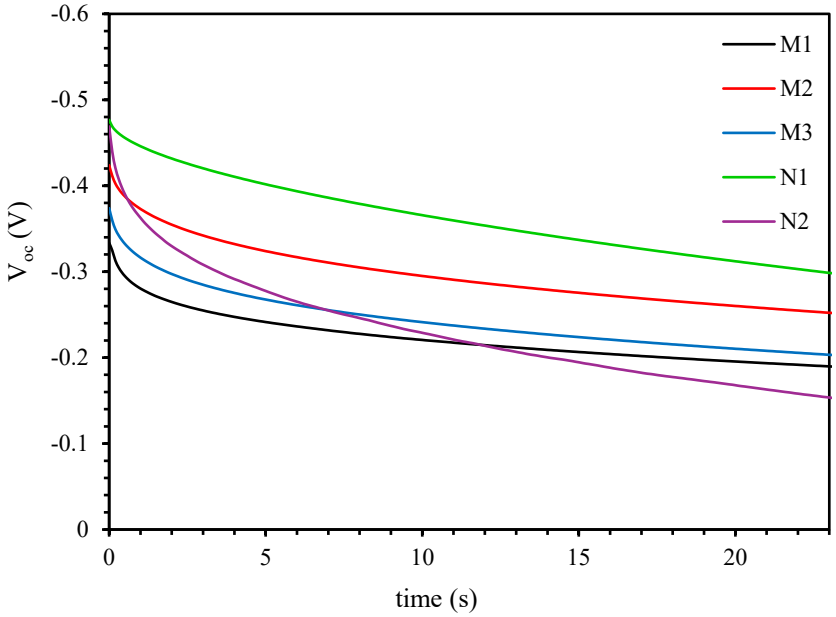

Figure 51. OCVD measurements of ssDSSCs M and N.

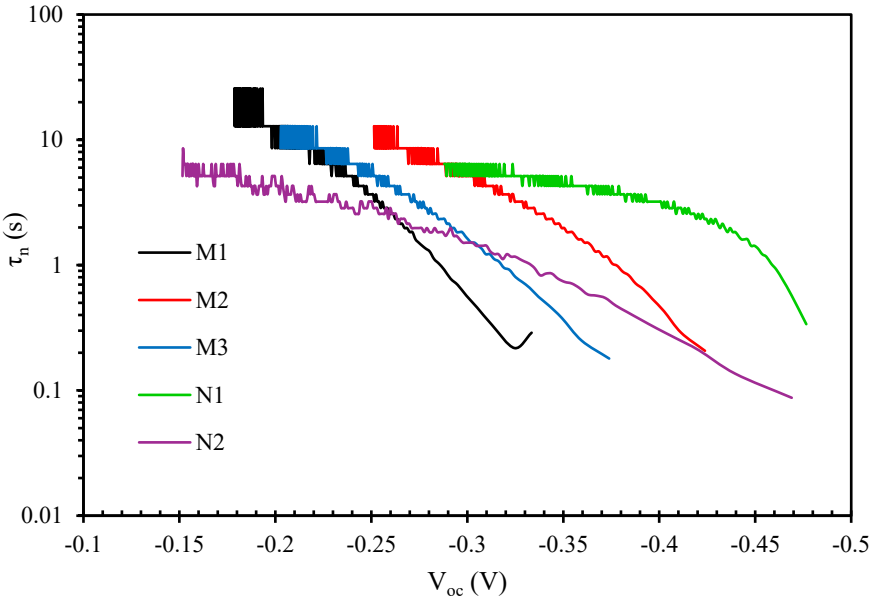

Figure 52. Lifetime measurements of ssDSSCs M and N.

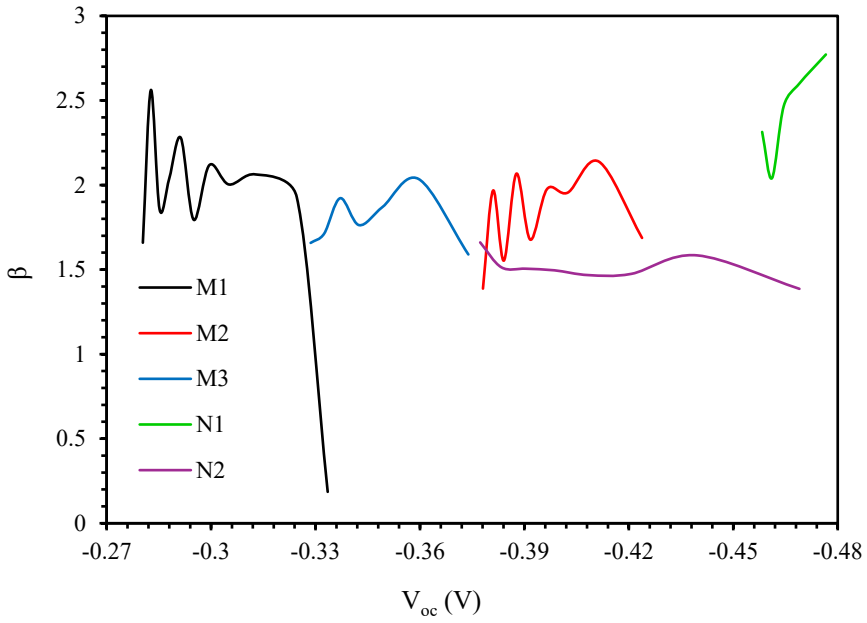

Figure 53. Recombination order of ssDSSCs M1-N2.

The presence of multiple recombination mechanisms in ssDSSC O are supported by the OCVD, τ_n and β measurements in figures 54, 55 and 56. A β of ~0.96-1.5 indicates a mostly trap-mediated process. Although the JV curves in figure 43 demonstrate ssDSSC P exhibited superior V_{oc}, J_{sc} and PCE relative to ssDSSC O, the initial V_{oc} of P in the OCVD plot was significantly lower than that of O. What's more, the V_{oc} increased over time. Multiple measurements of this specific solar cell were taken to confirm this behavior. Other solar cells of this type did not follow this behavior. I am unaware of any possible explanation and therefore τ_n and β measurements were excluded.

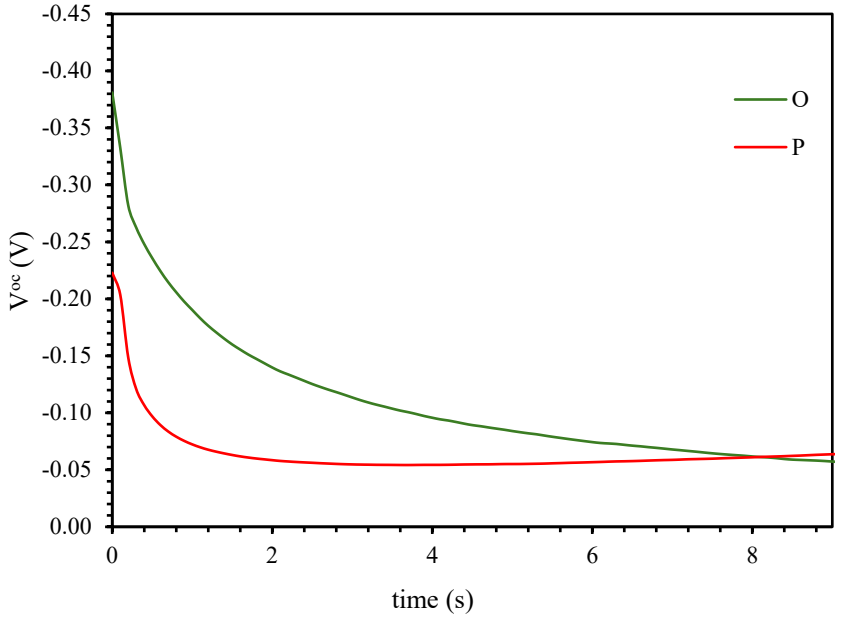

Figure 54. OCVD curves of ssDSSCs O and P.

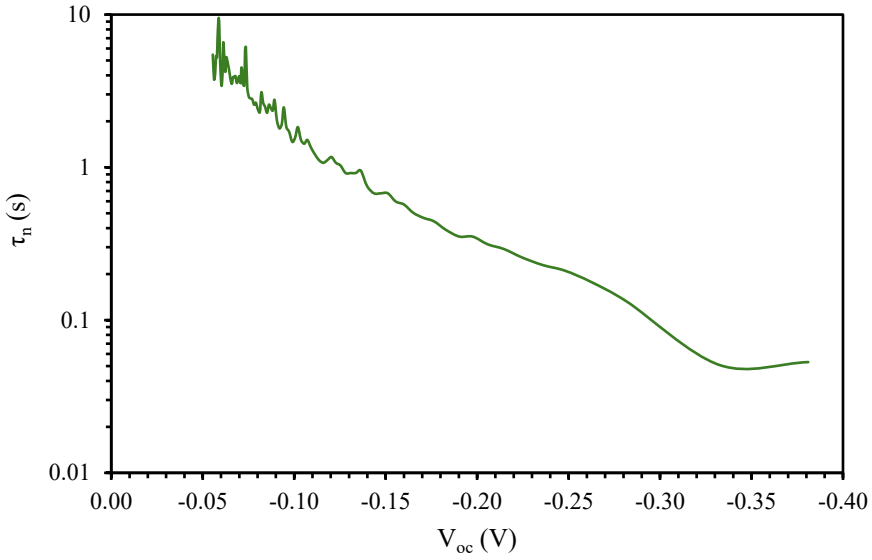

Figure 55. Lifetime measurements of ssDSSC O.

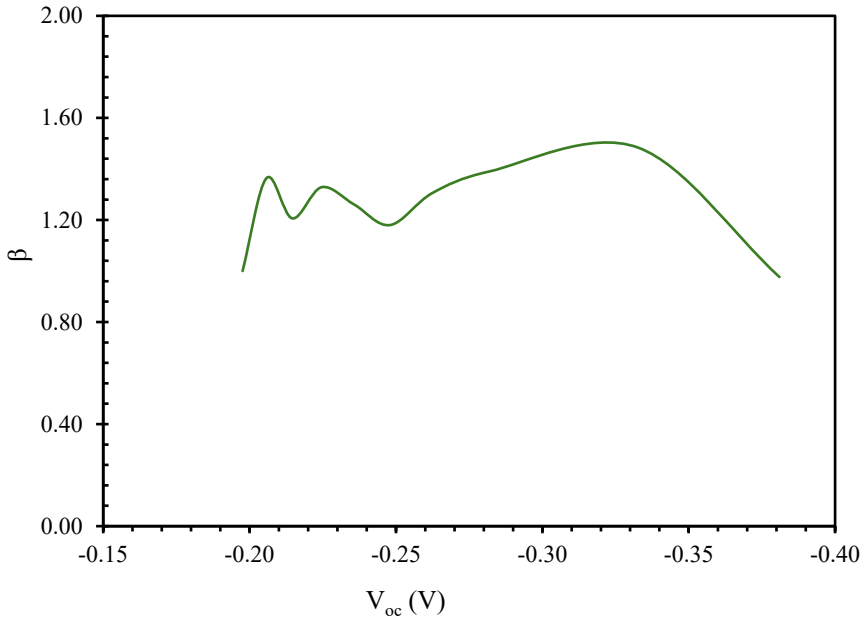

Figure 56. Recombination order of ssDSSC O.

Table 5. Different fabrication methods attempted. Layer deposition methods that are identical to those of the previous ssDSSC are omitted.

ssDSSC	Fabrication
A	• $TiO_{2\ comp}$: spin-coat at 2000 rpm, anneal 500 ºC (1 h) • 10 mM anchor (IPA): eqm. NaOH, submerge overnight (room temp.) • $[Ru^{II}\text{-tpy-ph-tpy}]_n(2Cl^-)_n$ (1 mM): evaporate completely (70 ºC) • HTM: spin-coat at 700-1000 rpm • Gold: sputter-coat 100 s
B	• 10 mM anchor (IPA): eqm. NaOH, submerge for 48 h (70 ºC) • $[Ru^{II}\text{-tpy-ph-tpy}]_n(2Cl^-)_n$ (1 mM): heat (70 ºC) until ~ 5 mL remain
C	• 1 mM anchor (EtOH): submerge for 24 h (room temp.) • $[Ru^{II}\text{-tpy-ph-tpy}]_n(2Cl^-)_n$ (1 mM): drop cast (room temp.)
D	• $[Ru^{II}\text{-tpy-ph-tpy}]_n(2PF_6^-)_n$ (1 mM): drop cast (room temp.)
E	• 1 mM anchor (EtOH): submerge for 24 h (80 ºC) • $[Ru^{II}\text{-tpy-ph-tpy}]_n(2Cl^-)_n$ (1 mM): evaporate completely (80 ºC)
F	• $TiO_{2\ comp}$: spin-coat at 2000 rpm, anneal 500 ºC (1 h) x 2 • 1.5 mM anchor (EtOH): submerge for 24 h (room temp.) • $[Ru^{II}\text{-tpy-ph-tpy}]_n(2Cl^-)_n$ (2 mM): drop cast (room temp.)
G	• $[Ru^{II}\text{-tpy-ph-tpy}]_n(2Cl^-)_n$ (2 mM): submerge for 24 h (room temp.)
H	• $[Ru^{II}\text{-tpy-ph-tpy}]_n(2Cl^-)_n$ (2 mM): evaporate completely (80 ºC)
I	• $TiO_{2\ comp}$: spin-coat at 2000 rpm, anneal 500 ºC (1 h) x 2 • 2 mM anchor (EtOH): room temperature soak • $[Ru^{II}\text{-tpy-ph-tpy}]_n(2Cl^-)_n$ (1 mM): drop cast (room temp.) • HTM: spin-coat at 2000 rpm • Gold: sputter-coat 150 s
J	• No anchor
K	• $TiO_{2\ comp}$: spin-coat at 2000 rpm, anneal 500 ºC (1 h) x 2 • 2 mM anchor (EtOH): room temperature soak • $[Ru^{II}\text{-tpy-ph-tpy}]_n(2PF_6^-)_n$ (1 mM): drop cast (room temp.) • HTM: spin-coat at 2000 rpm • Gold: sputter-coat 150 s
L	• No anchor
M	• $TiO_{2\ comp}$: spin-coat at 2000 rpm, anneal 500 ºC (12 h) x 2 (M1) • $TiO_{2\ comp}$: spin-coat at 2000 rpm, anneal 500 ºC (12 h) x 1 (M2, M3) • $TiO_{2\ part}$: spin-coat at 2000 rpm, anneal 500 ºC (12 h) x 1 (M2, M3) • 1.5 mM anchor (EtOH): eqm. KOH, submerge for 24 h (80-100 ºC) • $[Ru^{II}\text{-tpy-ph-tpy}]_n(2Cl^-)_n$ (0.3 mM): vapor diffusion (45 ºC) (M1, M2) • $[Ru^{II}\text{-tpy-ph-tpy}]_n(2Cl^-)_n$ (0.3 mM): heat in pressure vessel, 48 h (80 ºC) (M3) • Gold: sputter-coat 100 s
N	• $TiO_{2\ comp}$: spin-coat at 2000-3000 rpm, anneal 500 ºC (12 h) x 1 • $TiO_{2\ part}$: spin-coat at 2000-3000 rpm, anneal 500 ºC (12 h) x 1 • 5 mM anchor (EtOH): eqm. KOH, submerge for 24 h (80-100 ºC) • $[Ru^{II}\text{-tpy-ph-tpy}]_n(2Cl^-)_n$ (4.6 mM): drop cast (room temp.) (N1) • $[Ru^{II}\text{-tpy-ph-tpy}]_n(2Cl^-)_n$ (4.6 mM): hear in pressure vessel 48 h (90 ºC) (N2) • Gold: sputter-coat 130 s

O	• $TiO_{2\ comp}$: spin-coat at 2000-3000 rpm, anneal 500 ºC (12 h) x 1 • $TiO_{2\ part}$: air brush and spin-coat at 2000-3000 rpm, anneal 500 ºC (1 h) • 5 mM anchor (EtOH): eqm. KOH, submerge for 48 h when cells cool down to 80-100 ºC • $[Ru^{II}\text{-tpy-ph-tpy}]_n(2Cl^-)_n$ (6.5 mM): reflux under N_2 (g) in dry MeOH for 48 h (70 ºC) • HTM: spin-coat at 2000 rpms • Gold: sputter-coat 100 s
P	• $[Ru^{II}\text{-tpy-ph-tpy}]_n(2PF_6^-)_n$ (0.3 mM): reflux under N_2 (g) in dry acetonitrile for 48 h (90 ºC)

Table 6. Parameters of the best performing ssDSSCs of each type. The highest overall values are in red.

ssDSSC	V_{oc} (V) (dark)	J_{sc} (A cm^{-2}) (dark)	MP (W cm^{-2})	FF	Efficiency (%)
A	-0.49 (-0.17)	-3.14×10^{-6} (-1.54×10^{-6})	3.40×10^{-7}	0.22	2.48×10^{-4}
B1	-0.47 (-0.19)	-1.43×10^{-5} (-1.51×10^{-6})	1.03×10^{-6}	0.15	7.55×10^{-4}
B2	-0.27 (-0.002)	-3.74×10^{-5} (-2.17×10^{-7})	2.22×10^{-6}	0.22	1.62×10^{-3}
C1	-0.43 (-0.10)	-3.00×10^{-5} (-8.63×10^{-7})	2.28×10^{-6}	0.18	1.66×10^{-3}
C2	-0.55 (-0.06)	-1.19×10^{-5} (-9.12×10^{-7})	1.42×10^{-6}	0.23	1.03×10^{-3}
D1	-0.68 (-0.094)	-2.26×10^{-5} (-3.56×10^{-7})	3.01×10^{-6}	0.20	2.20×10^{-3}
D2	-0.71 (-0.249)	-1.46×10^{-5} (-8.42×10^{-7})	2.93×10^{-6}	0.28	2.14×10^{-3}
E	-0.71 (-0.38)	-7.36×10^{-6} (-7.27×10^{-7})	1.11×10^{-6}	0.21	8.14×10^{-4}
F	-0.55 (-0.22)	-2.32×10^{-5} (-1.74×10^{-6})	3.70×10^{-6}	0.29	2.70×10^{-3}
G	-0.32 (-0.03)	-3.33×10^{-5} (-2.93×10^{-6})	2.31×10^{-6}	0.22	1.69×10^{-3}
H	-0.53 (-0.21)	-1.60×10^{-5} (-5.71×10^{-6})	2.14×10^{-6}	0.25	1.56×10^{-3}

I	-0.66 (-0.26)	-3.04×10^{-5} (-3.15×10^{-6})	4.74×10^{-6}	0.24	3.46×10^{-3}
J	-0.64 (-0.01)	-4.41×10^{-5} (-4.77×10^{-7})	6.66×10^{-6}	0.24	4.86×10^{-3}
K	-0.48 (-0.02)	-3.90×10^{-5} (-1.31×10^{-6})	4.35×10^{-6}	0.23	3.17×10^{-3}
L	-0.50 (-0.01)	-4.59×10^{-5} (-7.90×10^{-7})	4.99×10^{-6}	0.22	3.64×10^{-3}
M1	-0.25 (-0.00)	-5.77×10^{-5} (-7.22×10^{-7})	3.12×10^{-6}	0.22	2.27×10^{-3}
M2	-0.36 (-0.07)	-1.19×10^{-4} (-9.63×10^{-6})	1.35×10^{-5}	0.32	9.86×10^{-3}
M3	-0.33 (-0.00)	-1.12×10^{-4} (-3.83×10^{-6})	1.16×10^{-5}	0.32	8.46×10^{-3}
N1	-0.34 (-0.09)	-4.51×10^{-6} (-1.55×10^{-6})	3.37×10^{-7}	0.22	2.46×10^{-4}
N2	-0.48 (-0.001)	-9.30×10^{-5} (-3.15×10^{-9})	1.47×10^{-5}	0.33	1.07×10^{-2}
O	-0.34 (-0.08)	-1.07×10^{-4} (-5.45×10^{-7})	1.33×10^{-5}	0.36	9.73×10^{-3}
P	-0.37 (-0.03)	-1.42×10^{-4} (-3.68×10^{-7})	2.22×10^{-5}	0.42	1.62×10^{-2}

CHAPTER 5

CONCLUSION AND FUTURE DIRECTIONS

The results show a feasible application of $[Ru^{II}\text{-tpy-ph-tpy}]_n(2X)_n$ as the photoactive material in ssDSSCs. UV-vis and CV were used to predict favorable orbital energy level alignment between the $[Ru^{II}\text{-tpy-ph-tpy}]_n(2X)_n$ LUMO and TiO_2 CB. Lower PCEs in early ssDSSCs (A-L) were due to high R_S in the thick $[Ru^{II}\text{-tpy-ph-tpy}]_n(2X)_n$ layers, the highest being $4.86x10^{-3}$% for ssDSSC J. This was supported by the prominent s-shaped JV curves in these types of cells, as well as decreased OCVD and longer τ_n; both of which are desired in high quality solar cells that are not affected by high R_S. The thick layers were a result of necessary drop casting or direct evaporation of $[Ru^{II}\text{-tpy-ph-tpy}]_n(2X)_n$ due to insufficient chemisorption between the anchor molecule and the $TiO_{2\ comp}$. Limited or no chemisorption at the $TiO_{2\ comp}$ surface hampered charge injection and was reflected as low J_{sc}, the highest being $-4.59x10^{-5}$ A cm^{-2} in solar cells that employed these deposition methods (ssDSSC L). However, these solar cells exhibited the highest V_{oc}'s likely due to suitable energy level alignment and high $TiO_{2\ comp}/[Ru^{II}\text{-tpy-ph-tpy}]_n(2X)_n$ contact. In the dropped casted solar cells, there were no significant differences in PCE and performance that can be attributed to varying the counterion between Cl^- and PF_6^-. Decreased solubility of $[Ru^{II}\text{-tpy-ph-tpy}]_n(2X)_n$ when $X = PF_6^-$ have been reported, therefore, visual differences in the sensitizer layer could be attributed to longer $[Ru^{II}\text{-tpy-ph-tpy}]_n(2X)_n$ monomers. The improved PCE via the inclusion of a $TiO_{2\ part}$ layer was likely due to improved adsorption of $[Ru^{II}\text{-tpy-ph-tpy}]_n(2X)_n$ through the anchor molecule. These ssDSSCs showed improvement in J_{sc} and FF. The decrease in V_{oc} can be

attributed to reduced $[Ru^{II}\text{-tpy-ph-tpy}]_n(2X)_n$ loading and therefore, future work should focus on increasing the $[Ru^{II}\text{-tpy-ph-tpy}]_n(2X)_n$ loading on $TiO_{2\ part}$ layer.

Future work should focus on improving the growth of $[Ru^{II}\text{-tpy-ph-tpy}]_n(2X)_n$ directly on the $TiO_{2\ part}$ by further improving current methods or through a layer-by-layer approach derived from methods described by Janini et al.[55] If the latter method is to be explored, understanding the long-range electron transport ability of $[Ru^{II}\text{-tpy-ph-tpy}]_n(2X)_n$ should be understood to determine the optimal amount of units needed to maximize absorbance and minimize R_S.

References

1. Copeland, A. W.; Black, O. D.; Garrett, A. B. The Photovoltaic Effect. *Chem. Rev.* **1942**, *31*, 177–226.

2. Paulescu, M.; Eugenia, P.; Gravila, P.; Badescu, V. *Weather Modeling and Forecasting of PV Systems Operation;* 2012; Vol. 103.

3. Wenham, S. R.; Green, M. A. Silicon solar cells. *Prog. Photovolt: Res. Appl.* **1996**, *4*, 3–33.

4. National Renewable Energy Laboratory Best Research-Cell Efficiency Chart. *https://www.nrel.gov/pv/cell-efficiency.html*.

5. Fraunhofer Institute for Solar Energy Systems ISE Fraunhofer ISE Develops the World's Most Efficient Solar Cell with 47.6 Percent Efficiency. *https://www.ise.fraunhofer.de/en/press-media/press-releases/2022/fraunhofer-ise-develops-the-worlds-most-efficient-solar-cell-with-47-comma-6-percent-efficiency.html* (accessed May 27, 2025).

6. Saga, T. Advances in crystalline silicon solar cell technology for industrial mass production. *NPG Asia Materials* **2010**, *2*, 96–102.

7. Yang, Y. M.; Yu, A.; Hsu, B.; Hsu, W. C.; Yang, A.; Lan, C. W. Development of high-performance multicrystalline silicon for photovoltaic industry. *Prog. Photovolt: Res. Appl.* **2015**, *23*, 340–351.

8. H. C. Card; E. S. Yang Electronic processes at grain boundaries in polycrystalline semiconductors under optical illumination. *IEEE Transactions on Electron Devices* **1977**, *24*, 397–402.

9. Ushasree, P. M.; Bora, B. Silicon Solar Cells. In *Solar Energy Capture Materials*; Gibson, E. A., Ed.; The Royal Society of Chemistry: 2019; pp 0.

10. AnonymousHow a Solar Cell Works. *https://www.acs.org/education/chemmatters/past-issues/archive-2013-2014/how-a-solar-cell-works.html* (accessed 12/03, 2024).

11. Benesperi, I.; Michaels, H.; Freitag, M. The researcher's guide to solid-state dye-sensitized solar cells. *J. Mater. Chem. C* **2018**, *6*, 11903–11942.

12. Aftabuzzaman, M.; Sarker, S.; Lu, C.; Kim, H. K. In-depth understanding of the energy loss and efficiency limit of dye-sensitized solar cells under outdoor and indoor conditions. *J. Mater. Chem. A* **2021**, *9*, 24830–24848.

13. Stockhausen, V.; Andrade, L.; Ivanou, D.; Stannowski, B.; Mendes, A. Incident Angle and Light Intensity Variation: a Comparative Impact Study on Perovskite, Dye-sensitized and Silicon Heterojunction Solar Cells Towards Building-Integrated Applications. *Solar Energy Mater. Solar Cells* **2019***, 191*, 451–458.

14. Hagfeldt, A.; Boschloo, G.; Sun, L.; Kloo, L.; Pettersson, H. Dye-Sensitized Solar Cells. *Chem. Rev.* **2010***, 110*, 6595–6663.

15. Sharma, K.; Sharma, V.; Sharma, S. S. Dye-Sensitized Solar Cells: Fundamentals and Current Status. *Nanoscale Research Letters* **2018***, 13*, 381.

16. O'Regan, B.; Grätzel, M. A low-cost, high-efficiency solar cell based on dye-sensitized colloidal TiO2 films. *Nature* **1991***, 353*, 737–740.

17. Wu, J.; Lan, Z.; Lin, J.; Huang, M.; Huang, Y.; Fan, L.; Luo, G. Electrolytes in Dye-Sensitized Solar Cells. *Chem. Rev.* **2015***, 115*, 2136–2173.

18. Ding, I.; Tétreault, N.; Brillet, J.; Hardin, B. E.; Smith, E. H.; Rosenthal, S. J.; Sauvage, F.; Grätzel, M.; McGehee, M. D. Pore-Filling of Spiro-OMeTAD in Solid-State Dye Sensitized Solar Cells: Quantification, Mechanism, and Consequences for Device Performance. *Adv. Funct. Mater.* **2009***, 19*, 2431–2436.

19. Listorti, A.; O'Regan, B.; Durrant, J. R. Electron Transfer Dynamics in Dye-Sensitized Solar Cells. *Chem. Mater.* **2011***, 23*, 3381–3399.

20. Tang, H.; Berger, H.; Schmid, P. E.; Lévy, F. Optical properties of anatase (TiO2). *Solid State Commun.* **1994***, 92*, 267–271.

21. Fondriest Environmental, I. Solar Radiation & Photosynthetically Active Radiation. *https://www.fondriest.com/environmental-measurements/parameters/weather/photosynthetically-active-radiation/* (accessed April 20, 2025).

22. Tétreault, N.; Arsenault, É; Heiniger, L.; Soheilnia, N.; Brillet, J.; Moehl, T.; Zakeeruddin, S.; Ozin, G. A.; Grätzel, M. High-Efficiency Dye-Sensitized Solar Cell with Three-Dimensional Photoanode. *Nano Lett.* **2011***, 11*, 4579–4584.

23. Tanvi; Mahajan, A.; Bedi, R. K.; Kumar, S.; Saxena, V.; Singh, A.; Aswal, D. K. Broadband enhancement in absorption cross-section of N719 dye using different anisotropic shaped single crystalline silver nanoparticles. *RSC Adv.* **2016***, 6*, 48064–48071.

24. Mukaddem, K. T.; Chater, P. A.; Devereux, L. R.; Al Bahri, O. K.; Jain, A.; Cole, J. M. Dye-Anchoring Modes at the Dye···TiO2 Interface of N3- and N749-Sensitized Solar Cells Revealed by Glancing-Angle Pair Distribution Function Analysis. *J. Phys. Chem. C* **2020***, 124*, 11935–11945.

25. Zhang, L.; Cole, J. M. Anchoring Groups for Dye-Sensitized Solar Cells. *ACS Appl. Mater. Interfaces* **2015***, 7*, 3427–3455.

26. Ardo, S.; Meyer, G. J. Photodriven heterogeneous charge transfer with transition-metal compounds anchored to TiO2 semiconductor surfaces. *Chem. Soc. Rev.* **2009***, 38*, 115–164.

27. Aftabuzzaman, M.; Sarker, S.; Lu, C.; Kim, H. K. In-depth understanding of the energy loss and efficiency limit of dye-sensitized solar cells under outdoor and indoor conditions. *J. Mater. Chem. A* **2021***, 9*, 24830–24848.

28. Aghazada, S.; Nazeeruddin, M. K. Ruthenium Complexes as Sensitizers in Dye-Sensitized Solar Cells. *Inorganics* **2018***, 6*.

29. Wu, K.; Hsu, H.; Chen, K.; Chi, Y.; Chung, M.; Liu, W.; Chou, P. Development of thiocyanate-free, charge-neutral Ru(ii) sensitizers for dye-sensitized solar cells. *Chem. Commun.* **2010***, 46*, 5124–5126.

30. Sun, Y.; Onicha, A. C.; Myahkostupov, M.; Castellano, F. N. Viable Alternative to N719 for Dye-Sensitized Solar Cells. *ACS Appl. Mater. Interfaces* **2010***, 2*, 2039–2045.

31. Listorti, A.; O'Regan, B.; Durrant, J. R. Electron Transfer Dynamics in Dye-Sensitized Solar Cells. *Chem. Mater.* **2011***, 23*, 3381–3399.

32. Cappel, U. B.; Gibson, E. A.; Hagfeldt, A.; Boschloo, G. Dye Regeneration by Spiro-MeOTAD in Solid State Dye-Sensitized Solar Cells Studied by Photoinduced Absorption Spectroscopy and Spectroelectrochemistry. *J. Phys. Chem. C* **2009***, 113*, 6275–6281.

33. Kroeze, J. ; Hirata, N.; Schmidt-Mende, L.; Orizu, C.; Ogier, S. ; Carr, K.; Grätzel, M.; Durrant, J. Parameters Influencing Charge Separation in Solid-State Dye-Sensitized Solar Cells Using Novel Hole Conductors. *Adv. Funct. Mater.* **2006***, 16*, 1832–1838.

34. Burschka, J.; Kessler, F.; Nazeeruddin, M. K.; Grätzel, M. Co(III) Complexes as p-Dopants in Solid-State Dye-Sensitized Solar Cells. *Chem. Mater.* **2013***, 25*, 2986–2990.

35. Zaban, A.; Greenshtein, M.; Bisquert, J. Determination of the Electron Lifetime in Nanocrystalline Dye Solar Cells by Open-Circuit Voltage Decay Measurements. *ChemPhysChem* **2003***, 4*, 859–864.

36. Amadelli, R.; Argazzi, R.; Bignozzi, C. A.; Scandola, F. Design of antenna-sensitizer polynuclear complexes. Sensitization of titanium dioxide with [Ru(bpy)2(CN)2]2Ru(bpy(COO)2)22-. *J. Am. Chem. Soc.* **1990***, 112*, 7099–7103.

37. Yu, Q.; Liu, S.; Zhang, M.; Cai, N.; Wang, Y.; Wang, P. An Extremely High Molar Extinction Coefficient Ruthenium Sensitizer in Dye-Sensitized Solar Cells: The Effects of π-Conjugation Extension. *J. Phys. Chem. C* **2009**, *113*, 14559–14566.

38. Vaduvescu, S.; Potvin, P. G. Linear Multinuclear RuII Photosensitizers. *Eur. J. Inorg. Chem.* **2004**, *2004*, 1763–1769.

39. Vaduvescu, S.; Potvin, P. G. Synthesis and Characterization of a Novel Linear Trinuclear Ruthenium(II) Complex: Variation of Photosensitization Ability with Chain Length in a Homologous Series. *Inorg. Chem.* **2002**, *41*, 4081–4083.

40. Han, F. S.; Higuchi, M.; Ikeda, T.; Negishi, Y.; Tsukuda, T.; Kurth, D. G. Luminescence properties of metallo-supramolecular coordination polymers assembled from pyridine ring functionalized ditopic bis-terpyridines and Ru(ii) ion. *J. Mater. Chem.* **2008**, *18*, 4555–4560.

41. Pei, J.; Huang, X.; Zhao, X.; Lv, H.; Chen, S.; Zhang, S.; Li, Y.; Hao, Y. Hybrid solar cells of Ru-based dye complexes as interfacial modification layers: Energy level alignment and photoelectric properties improvement. *Surfaces and Interfaces* **2021**, *23*, 100981.

42. Zanzi, J.; Pastorel, Z.; Duhayon, C.; Lognon, E.; Coudret, C.; Monari, A.; Dixon, I. M.; Canac, Y.; Smietana, M.; Baslé, O. Counterion Effects in [Ru(bpy)3](X)2-Photocatalyzed Energy Transfer Reactions. *JACS Au* **2024**, *4*, 3049–3057.

43. Han, F. S.; Higuchi, M.; Kurth, D. G. Metallosupramolecular Polyelectrolytes Self-Assembled from Various Pyridine Ring-Substituted Bisterpyridines and Metal Ions: Photophysical, Electrochemical, and Electrochromic Properties. *J. Am. Chem. Soc.* **2008**, *130*, 2073–2081.

44. Higuchi, M. Electrochromic Organic–Metallic Hybrid Polymers: Fundamentals and Device Applications. *Polym. J.* **2009**, *41*, 511–520.

45. Elgrishi, N.; Rountree, K. J.; McCarthy, B. D.; Rountree, E. S.; Eisenhart, T. T.; Dempsey, J. L. A Practical Beginner's Guide to Cyclic Voltammetry. *J. Chem. Educ.* **2018**, *95*, 197–206.

46. PINE Research Referencing Electrochemical Data to an Internal Standard. https://pineresearch.com/support-article/reference-to-an-internal-standard/ (accessed May 27, 2025).

47. Rana, U.; Santra, D. C.; Prusti, B.; Chakraborty, C.; Ikeda, T.; Saito, Y.; Takeuchi, K.; Nagahata, R.; Higuchi, M. Microwave-Assisted Quick Synthesis of Ru(II)-Based Metallosupramolecular Polymer for Improved Electrochromic Properties. *Macromol. Chem. Phys.* **2024**, *225*, 2300381.

48. Fu, X.; Zhang, Z.; Cao, Z.; Rogachev, A. A.; Yarmolenko, M. A.; Chen, T.; Cao, H.; Zhang, H. Mechanistic Insights into Anion-Induced Electrochromism of Ru(II)-Based Metallo-Supramolecular Polymer. *Polymers* **2023***, 15*.

49. Kokkonen, M.; Talebi, P.; Zhou, J.; Asgari, S.; Soomro, S. A.; Elsehrawy, F.; Halme, J.; Ahmad, S.; Hagfeldt, A.; Hashmi, S. G. Advanced research trends in dye-sensitized solar cells. *J. Mater. Chem. A* **2021***, 9*, 10527–10545.

50. Zhang, J.; Yu, C.; Wang, L.; Li, Y.; Ren, Y.; Shum, K. Energy barrier at the N719-dye/CsSnI3 interface for photogenerated holes in dye-sensitized solar cells. *Scientific Reports* **2014***, 4*, 6954.

51. Rombach, F. M.; Haque, S. A.; Macdonald, T. J. Lessons learned from spiro-OMeTAD and PTAA in perovskite solar cells. *Energy Environ. Sci.* **2021***, 14*, 5161–5190.

52. Saive, R. S-Shaped Current–Voltage Characteristics in Solar Cells: A Review. *IEEE Journal of Photovoltaics* **2019***, 9*, 1477–1484.

53. Jiang, D.; Hao, Y.; Shen, R.; Ghazarian, S.; Ramos, A.; Zhou, F. Effective Blockage of the Interfacial Recombination Process at TiO2 Nanowire Array Electrodes in Dye-Sensitized Solar Cells. *ACS Appl. Mater. Interfaces* **2013***, 5*, 11906–11912.

54. Vollbrecht, J.; Brus, V. V. Effects of Recombination Order on Open-Circuit Voltage Decay Measurements of Organic and Perovskite Solar Cells. *Energies* **2021***, 14*.

55. Janini, T. E.; Fattore, J. L.; Mohler, D. L. Rapid assembly of rigid rods by metal complexation of bis(terpyridyl) ligands. *Journal of Organometallic Chemistry* **1999***, 578*, 260–263.